Structural and dynamic changes in P-Rex1 upon activation by PIP_3 and inhibition by IP_4

Sandeep K. Ravala[1], Sendi Rafael Adame-Garcia[2], Sheng Li[3], Chun-Liang Chen[1], Michael A. Cianfrocco[4], J. Silvio Gutkind[2], Jennifer N. Cash*[5], and John J. G. Tesmer*[1]

[1]Departments of Biological Sciences and of Medicinal Chemistry and Molecular Pharmacology, Purdue University, West Lafayette, Indiana 47907, United States

[2]Department of Pharmacology and Moores Cancer Center, University of California, San Diego, San Diego, CA 92093, USA

[3]Department of Medicine, University of California San Diego, La Jolla, CA 92093, USA.

[4]Department of Biological Chemistry, University of Michigan, Ann Arbor, Michigan 48109, United States

[5]Department of Molecular and Cellular Biology, University of California-Davis, Davis, CA, 95616, USA.

*To whom correspondence should be addressed: jcash@ucdavis.edu and jtesmer@purdue.edu

Abstract

PIP_3-dependent Rac exchanger 1 (P-Rex1) is abundantly expressed in neutrophils and plays central roles in chemotaxis and cancer metastasis by serving as a guanine-nucleotide exchange factor (GEF) for Rac. The enzyme is synergistically activated by PIP_3 and the heterotrimeric Gβγ subunits, but mechanistic details remain poorly understood. While investigating the regulation of P-Rex1 by PIP_3, we discovered that Ins(1,3,4,5)P_4 (IP_4) inhibits P-Rex1 activity and induces large decreases in backbone dynamics in diverse regions of the protein. Cryo-electron microscopy analysis of the P-Rex1·IP_4 complex revealed a conformation wherein the pleckstrin homology (PH) domain occludes the active site of the Dbl homology (DH) domain. This configuration is stabilized by interactions between the first DEP domain (DEP1) and the DH domain and between the PH domain and a 4-helix bundle (4HB) subdomain that extends from the C-terminal domain of P-Rex1. Disruption of the DH–DEP1 interface in a DH/PH-DEP1 fragment enhanced activity and led to a more extended conformation in solution, whereas mutations that constrain the occluded conformation led to decreased GEF activity. Variants of full-length P-Rex1 in which the DH–DEP1 and PH–4HB interfaces were disturbed exhibited enhanced activity during chemokine-induced cell migration, confirming that the observed structure represents the autoinhibited state in living cells. Interactions with PIP_3-containing liposomes led to disruption of these interfaces and increased dynamics protein-wide. Our results further suggest that inositol phosphates such as IP_4 help to inhibit basal P-Rex1 activity in neutrophils, similar to their inhibitory effects on phosphatidylinositol-3-kinase.

38 **Introduction**

39 Localized activation of signaling is required for proper cell migration. Phosphatidylinositol 3,4,5-
40 trisphosphate (PIP_3)-dependent Rac exchanger 1 (P-Rex1) is a Rho guanine-nucleotide exchange
41 factor (RhoGEF) abundantly expressed in neutrophils that mediates chemotaxis and the generation
42 of reactive oxygen species via activation of Rac GTPases (Dorseuil et al., 1992). The protein is
43 comprised of a catalytic Dbl homology (DH) domain followed by a pleckstrin homology (PH)
44 domain, two DEP domains (DEP1 and DEP2), two PDZ domains (PDZ1 and PDZ2), and a C-
45 terminal inositol polyphosphate-4-phosphatase-like (IP4P) domain (Fig. 1A).

46 P-Rex1 exhibits low basal activity until it becomes activated via direct interaction with
47 membrane-bound regulators PIP_3 and Gβγ which act synergistically (Cash et al., 2019, 2016;
48 Mayeenuddin et al., 2006; Welch et al., 2002), indicating that they use distinct modes of regulation.
49 Although relatively little is known about how P-Rex1 transitions to an activated state, recent
50 structural studies have defined their docking sites. Gβγ engages a scaffold composed of an
51 amalgamation of the DEP2-PDZ1-PDZ2-IP4P domains and likely helps recruit P-Rex1 to the cell
52 membrane (Cash et al., 2019). In contrast, PIP_3 binds to the PH domain (Hill et al., 2005) in a basic
53 pocket (Cash et al., 2016), but this is not necessary for its recruitment to the cell membrane,
54 implying that PIP_3 instead induces a conformational change that activates the enzyme (Cash et al.,
55 2016). Because domains C-terminal to the catalytic DH domain are well known to be involved in
56 autoinhibition (Chávez-Vargas et al., 2016; Hill et al., 2005; Ravala et al., 2020; Urano et al.,
57 2008), the allosteric change induced by PIP_3 must defeat interdomain contacts and render the
58 catalytic DH domain accessible to its substrate.

59 Here, we used hydrogen-deuterium exchange mass spectrometry (HDX-MS), cryo-
60 electron microscopy (cryo-EM) single particle analysis (SPA), and small-angle X-ray scattering

61 (SAXS) along with functional studies and live cell experiments to show that activation of P-Rex1
62 involves disruption of two different inhibitory interfaces between domains across the length of the
63 protein. Surprisingly, we found that the PIP_3 headgroup analog IP_4 can reduce P-Rex1 activity by
64 stabilizing the autoinhibited conformation of the enzyme at physiologically relevant
65 concentrations, suggesting a previously unknown, additional mechanism of regulation. Our
66 experiments further suggest that P-Rex1 binding to PIP_3-containing membranes induces
67 conformational changes that unwind P-Rex1 into a fully active state.
68
69 **Results**
70 *IP_4 induces protection from deuterium incorporation on regions of P-Rex1 distal from the PIP_3-*
71 *binding site.*
72 Previous work suggested that PIP_3 binding to the PH domain activates P-Rex1 purely through an
73 allosteric mechanism (Cash et al., 2016). Thus, we anticipated that binding of the soluble
74 headgroup of PIP_3, IP_4, to full-length P-Rex1 could also lead to conformational changes
75 characteristic of the activated state. To test this, we analyzed P-Rex1 in the presence and absence
76 of IP_4 using HDX-MS. We observed strong protection from deuterium incorporation in the PIP_3-
77 binding site on the PH domain in the presence of IP_4 (Fig. 1A&B, Sup. Data 1). However, we also
78 observed strong protection in other regions of the protein: namely on the surface of the PH domain,
79 particularly in the β5/β6 loop, and in several regions within an extension of the C-terminal IP4P
80 domain that was not visualized in the P-Rex1–Gβγ complex (Fig. 1A&C) (Cash et al., 2019). We
81 speculated that these diverse regions form more stable long-range interactions in the presence of
82 IP_4.
83

84 *IP_4 allosterically inhibits P-Rex1.*

85 Based on our HDX-MS data, we hypothesized that IP_4 could inhibit activity of full-length P-Rex1.
86 Using an *in vitro* GEF activity assay on soluble Cdc42 in the presence of liposomes, we observed
87 that IP_4 inhibits PIP_3-mediated activation of P-Rex1 with an IC_{50} value of 1.4 μM (Fig. 1D).
88 Competition was not observed with Ins(1,4,5)P_3, indicating that inhibition is dependent on the 3-
89 phosphate, which is critical for PIP_3 binding to the P-Rex1 PH domain (Cash et al., 2016).
90 However, IP_4 did not affect the activity of the P-Rex1 DH/PH or DH/PH-DEP1 fragments (Sup.
91 Fig. 1A&B). Collectively, these results indicated that IP_4 inhibits P-Rex1 allosterically and that
92 this inhibition is dependent on long range interactions between the regions shown to be protected
93 by IP_4 in the Gβγ-binding scaffold (DEP2-PDZ1-PDZ2-IP4P) and in the DH/PH-DEP1 module.
94 Negatively charged liposomes (containing PC/PS), including those that also contain PIP_3, inhibit
95 the GEF activity of the DH/PH-DEP1 and DH/PH fragments (Sup. Fig. 1C). Because full-length
96 P-Rex1 is not affected by PC/PS liposomes, this suggests that the observed inhibition represents a
97 non-productive interaction of the DH/PH-DEP1 and DH/PH fragments with negatively charged
98 surfaces in our assay. The lack of activation of DH/PH-DEP1 by PIP_3 prevents us from testing in
99 this assay whether IP_4 can inhibit via direct competition with PIP_3 at the PH domain.

100

101 *IP_4 stabilizes long-range interactions mediated by the P-Rex1 DEP1 and PH domains.*

102 To understand the molecular basis of IP_4-mediated stabilization and inhibition, we analyzed full-
103 length P-Rex1 with and without IP_4 using cryo-EM SPA (Sup. Fig. 2A). Initial datasets were
104 collected using a Glacios transmission electron microscope and then processed through 2D
105 classification (Sup. Fig. 2B-D). In both datasets, most classes showed only the Gβγ-binding core
106 of P-Rex1 (Sup. Fig. 2C&D). A few classes contained particles with additional mass to the side of

107 the core, close to the PDZ or DEP domains (Sup. Fig. 2C&D, orange boxes). This mass could
108 represent either the N-terminal domains or another P-Rex1 particle in proximity. Only in the
109 sample containing IP_4 could we observe class averages with additional mass next to the core
110 opposite the side that binds Gβγ (Sup. Fig. 2D, green boxes). Based on its size, location, our HDX-
111 MS data (Fig. 1), and low-resolution maps of P-Rex1 generated in a previous study (Cash et al.,
112 2019), this mass most likely corresponded to the N-terminal DH/PH-DEP1 domains interacting
113 with an elongated subdomain extending from the IP4P domain.

114 We next collected much larger datasets on the P-Rex1·IP_4 complex using a Krios
115 transmission electron microscope and determined the structure of this complex at an average
116 resolution of 4.1 Å (Fig. 2A-B, Table 1, and Sup. Fig. 3). Similar to the P-Rex1–Gβγ complex
117 (Cash et al., 2019), this sample exhibited a preferred orientation on grids, necessitating the addition
118 of data collected on a tilted sample (Sup. Fig. 3A,C). The resulting 3D reconstruction clearly shows
119 the Gβγ-binding core, composed of DEP2, PDZ1, PDZ2, and the majority of the IP4P domain,
120 from which there are two extensions of density that contact one another to form a loop-like
121 structure (Fig. 2A and Sup. Fig. 3D). One extension corresponds to a large insertion in the IP4P
122 domain that contains IP_4-stabilized regions (Fig. 1) and that was disordered in the P-Rex1–Gβγ
123 complex (Cash et al., 2019). The ordered elements of the insertion form a long 4-helix bundle
124 (4HB) most similar in fold to focal adhesion targeting (FAT) domains (Hayashi et al., 2002), which
125 are found in other peripheral membrane proteins involved in cell adhesion and migration. The
126 other extension corresponds to the DH/PH-DEP1 domains. Based on its distinct shape, the PH
127 domain (Cash, 2016) was fit into density along the side of the 4HB. Here, IP_4 is observed bound
128 to the PH domain PIP_3-binding site (Fig. 4B). The position of the DH domain was also obvious,
129 but individual helices of the DH domain were lower in resolution and more dynamic relative to

130 the rest of the structure (Sup. Fig. 3D). The relative positions of the DH and PH domains mandate
131 a severe bend in the helix connecting the DH and PH domains (Fig. 2A&B), resulting in a jack-
132 knifed configuration of the DH/PH module that blocks access to the GTPase binding site on the
133 DH domain. The remaining mass, immediately adjacent to the end of the DH domain opposite its
134 N-terminus, corresponds to DEP1. Using the required connectivity of its N- and C-termini to the
135 PH and DEP2 domains, respectively, DEP1 was docked in a manner that complemented residues
136 on the DH domain and corroborated the HDX-MS data (Fig. 4A). Weak density corresponding to
137 a long 5-turn extension of the αC helix of the PH domain connects to the N-terminus of DEP1, but
138 its C-terminal connection to DEP2 is disordered, likely explaining lower local resolution in the
139 DEP1 region (Sup. Fig. 3D). Overall, the conformation of the P-Rex1 Gβγ-binding core is
140 essentially the same as in the P-Rex1–Gβγ complex (RMSD deviation of 1.1 Å for 701 Cα atoms).
141 The contact between the PH domain and the 4HB is primarily mediated via the β1 and β2
142 strands and β5/β6 loop of the PH domain (Fig. 2C&D). In all previous crystal structures including
143 the P-Rex1 PH domain, this same surface formed extensive protein-protein lattice contacts (Cash
144 et al., 2016; Lucato et al., 2015). The residues directly involved in the interface are among the most
145 strongly protected in the presence of IP_4 as measured by HDX-MS (Fig. 1A-C, Fig. 4A). The PH
146 domain β3/β4 loop, which we previously showed to be a nonspecific anionic membrane-binding
147 loop, remains unstructured and is situated near a loop at the tip of the 4HB that is also unstructured
148 (residues 1109-1209, Fig. 2C) and contains known phosphorylation sites, some of which regulate
149 activity (Barber et al., 2012). At the interface, surface hydrophobic residues Leu279 and Ile286 on
150 the PH β1 and β2 strands and Tyr353 on the β5/β6 loop interact with a surface of 4HB including
151 Tyr1096 and His1224 (Fig. 2D). Charge complementarity is formed between Lys302 in the PH
152 domain and Asp1216 in 4HB, and between the 1-phosphate of IP_4 and Lys1217. Otherwise, IP_4

153 does not make direct contact with the 4HB. However, because different PH domain ligands
154 uniquely perturb the conformation of these regions in the PH domain (Cash et al., 2016), IP_4 could
155 indirectly stabilize this interface by trapping the β1 and β2 strands and β5/β6 loop in a
156 conformation with higher affinity for 4HB.

157 The jack-knife in the helix between the DH and PH domains is required to allow the PH
158 domain to interact with the 4HB and is stabilized by the DEP1 domain docking to the DH domain
159 (Fig. 2B). DH domain residues Leu173, Leu177, and Leu178 form a hydrophobic interface with
160 DEP1 residues Ile409, Ile457, Leu466, and Ala469 (Fig. 3A). Leu173 and Leu177 were previously
161 noted to be conspicuously exposed in structures of the DH/PH tandem (Cash et al., 2016). Thus,
162 the DEP1 domain stabilizes an inactive DH/PH tandem that is further stabilized by interaction with
163 the 4HB of the IP4P domain.

164 While conducting these studies, the structure of human P-Rex1 in the absence of IP_4 was
165 reported (PDB entry 7SYF) (Chang et al., 2022), allowing a comparison between the IP_4 and IP_4-
166 free states of autoinhibited P-Rex1 (Sup. Fig. 5). Overall, the domain organization is very similar,
167 but there is an ~3˚ rotation of the Gβγ-binding core in the IP_4 complex relative to the PH–4HB
168 interface such that DEP1 and DEP2 move closer together. It is possible that the binding of IP_4 at
169 this interface drives this conformational change. A caveat is that the protein used for the 7SYF
170 structure contained a T4 lysozyme domain inserted into the β3/β4 loop of the PH domain. Although
171 this domain was not visible in the reconstruction, its proximity to the IP_4 binding site may influence
172 the global conformation of P-Rex1. The similarities between P-Rex1±IP_4 also suggest that the IP_4-
173 binding site in the PH domain is freely accessible in the autoinhibited state. PIP_3 would, however,
174 not have access because the 4HB domain would block binding to a membrane surface.
175

176 *The DH–DEP1 interface contributes to autoinhibition in vitro.*

177 To test the contribution of the observed DH–DEP1 interface to autoinhibition, the interface was
178 disrupted by site-directed mutagenesis in the context of the DH/PH-DEP1 fragment. This fragment
179 is 5- to 10-fold less active (depending on assay conditions) than the DH/PH tandem alone (Sup.
180 Fig. 1C) (Ravala et al., 2020), confirming a specific role for DEP1 in autoinhibition (Fig. 3C).
181 Single point mutations in the interface profoundly affected GEF activity on soluble Cdc42. The
182 L173A variant had ~2.5-fold higher activity, whereas L177E and L178E exhibited 4- to 5-fold
183 higher activity, similar to the activity of DH/PH without the DEP1 domain. In the DEP1 domain,
184 I409A and L466A mutations resulted in ~2- and 4-fold higher activity, respectively. The α1/α2
185 loop (residues 77-90) of the DH domain, although ordered in previous structures of DH/PH bound
186 to GTPases (Cash et al., 2016; Lucato et al., 2015), is disordered in our structure (Fig. 3B).
187 However, modeling the DH domain from previous DH/PH crystal structures suggests that Lys89
188 and Arg78 would be close enough to form a bipartite ionic interaction with Glu456 in the DEP1
189 domain. Consistent with this hypothesis, the E456K variant was ~2.5-fold more active.
190 Surprisingly, one of the intended disruptive mutations, A170K, instead inhibited GEF activity by
191 ~50% (Fig. 3C). Based on the available structures, Lys170 in the DH domain could form
192 complementary electrostatic interactions with Glu411 along with additional non-polar interactions
193 with the backbone and side chains of residues 409, 411, and 412 in the DEP1 domain, thereby
194 stabilizing the DH–DEP1 interface (Fig. 3B).

195

196 *The DH—DEP1 interface stabilizes DH/PH-DEP1 and decreases flexibility.*

197 Because disruption of the DH–DEP1 interface led to increased activity, we predicted that these
198 variants would have a more extended DH/PH module that is likely more dynamic. To test this,

199 wild-type (WT) DH/PH-DEP1 and its variants were assessed using a ThermoFluor assay to
200 determine their melting temperatures (T_m). Indeed, variants with increased activity also had lower
201 T_m values (Fig. 3D, Table 2). Conversely, A170K, which was less active than WT, showed a higher
202 T_m. We also analyzed these variants using size exclusion chromatography coupled to small-angle
203 X-ray scattering (SEC-SAXS) (Sup. Fig. 6A&B). In previous SAXS analyses, we observed that
204 DH/PH-DEP1 exhibited a more compact state with a smaller conformational landscape in solution
205 relative to DH/PH (Ravala et al., 2020). We hypothesized that mutations which disrupt the DH–
206 DEP1 interface would likewise lead to more elongated ensembles. Compared to WT DH/PH-
207 DEP1, which had a radius of gyration (R_g) of 30 ± 0.3 Å, the L177E variant (the most active
208 DH/PH-DEP1 variant tested) had an R_g of 31 ± 0.2 Å, suggestive of expansion (Fig. 3E and Table
209 3). Variants A170K and I409A had R_g values similar to that of WT. Kratky plots indicated that all
210 the samples had heterogeneous conformations (Sup. Fig. 6C). The shapes of the P(r) functions
211 were similar for all variants except a longer tail for L177E and I409A, consistent with a higher
212 proportion of extended conformations in solution (Sup. Fig. 6D).

213 Because the samples exhibited a high degree of heterogeneity in solution, the
214 conformational distribution of these variants was assessed using the ensemble optimization method
215 (EOM) (Fig. 3E&F, Sup. Fig. 6A) (Tria et al., 2015). The resulting ensemble for WT shows
216 predominant conformations with R_g values ~ 28 Å and a small fraction of extended conformations
217 with R_g ~ 39 Å (Fig. 3E). The selected ensemble for A170K had R_g values similar to WT (~29 Å),
218 however the A170K peak is broader in comparison, suggesting conformational heterogeneity and
219 structural changes. The L177E variant exhibited a larger shift to higher R_g, with an average R_g ~
220 30 Å, and a second significant population with R_g > 32 Å (Fig. 3E). Similar to the distribution of
221 R_g values, the D_{max} function distribution shows that the L177E variant had the most extended

222 conformation of the variants tested (Fig. 3F). Other analyses were also consistent with L177E
223 being the most flexible and extended variant (see methods).
224
225 *Flexibility of the hinge in the α6-αN helix of the DH/PH module is important for autoinhibition.*
226 One of our initial goals in this project was to determine a high-resolution structure of the
227 autoinhibited DH/PH-DEP1 core by X-ray crystallography. To this end, we started with the
228 DH/PH-DEP1 A170K variant, which was more inhibited than wild-type but still dynamic, and then
229 introduced S235C/M244C and K207C/E251C double mutants to completely constrain the hinge
230 in the α6-αN helix via disulfide bond formation in a redox sensitive manner. Single cysteine
231 variants K207C and M244C were generated as controls. The S235C/M244C variant performed as
232 expected, decreasing the activity of the A170K variant to nearly background in the oxidized but
233 not the reduced state (Sup. Fig. 4). However, the M244C single mutant exhibited similar effects,
234 suggesting that it forms disulfide bonds with cysteine(s) other than S235C. Indeed, the side chains
235 of Cys200 and Cys234 are very close to that of M244C. The K207C/E251C mutant was similar to
236 S235C/M244C under oxidized conditions, but ~15-fold more active (similar to WT DH/PH levels,
237 see Fig. 3C) under reducing conditions. The K270C variant, on the other hand, exhibited higher
238 activity than A170K on its own under oxidizing conditions, but similar activity to all the variants
239 except K207C/E251C when reduced. These results suggest that K207C/E251C in a reduced state
240 and K270C in an oxidized state favor a configuration where the DEP1 domain is less able to engage
241 the DH domain and maintain the kinked state. The mechanism for this is not known. Regardless,
242 these data show that perturbation of contacts between the kinked segments of the α6-αN helix can
243 have profound consequences on the activity of the DH/PH-DEP1 core.
244

245 *Interactions at the P-Rex1 DH–DEP1 and PH–4HB interfaces contribute to autoinhibition in cells.*
246 To evaluate the roles of the P-Rex1 DH–DEP1 and PH–4HB interfaces in living cells, we utilized
247 SRE luciferase-gene reporter assays as a read out of full-length P-Rex1 activity in HEK293T cells.
248 Mutations at the DH–DEP1 interface had a strong effect on activity, with L177E and L466E (Fig.
249 3A) exhibiting ~10-fold and ~4-fold higher activity relative to WT, respectively (Fig. 5A).
250 Perturbation of the PH–4HB interface (Fig. 2D) also increased activity in that Y1096A was ~5-
251 fold more active than WT (Fig. 5A). Mutation of other residues in the PH–4HB interface (Fig. 2D)
252 also increased activity, although to a lesser extent.
253 The most affected variants (L177E, L466E, and Y1096A) were then tested for their effects
254 on cell migration in response to chemokine gradients (Fig. 5B&C, Sup. Fig. 7A&B). For this, the
255 endogenous P-Rex1 gene in HeLa cells was first knocked out by CRISPR-Cas9 (Sup. Fig. 7C) and
256 the resulting cells were transfected with various P-Rex1 constructs (Sup. Fig. 7D). Cell migration
257 was then evaluated in the presence or absence of CXCL12 (upstream of P-Rex1 and Gβγ signaling)
258 and epidermal growth factor (EGF). CXCL12-induced chemotaxis was dependent on the
259 expression of P-Rex1 (Fig. 5B&C and Sup. Fig. 7), and all three variants caused a significantly
260 larger number of cells to migrate. However, EGF-induced chemotaxis in HeLa cells, which is not
261 dependent on P-Rex1, was unaffected by P-Rex1 expression. These data support that the DH–
262 DEP1 and PH–4HB interfaces of P-Rex1 mediate autoinhibition that specifically modulates
263 chemokine-induced cell migration.
264
265 *P-Rex1 binding to PIP_3-containing model membranes induces a more open, dynamic*
266 *conformation.*

267 Given the known binding site for Gβγ (Cash et al., 2019), the position of membrane-binding loops
268 such as the β1/β2 loop of the DEP1 domain (Ravala et al., 2020), and the position of the 4HB
269 domain, it does not seem that the PH domain would be able to interact with PIP_3 in a cell membrane
270 while P-Rex1 is in its autoinhibited conformation. To better understand the molecular
271 consequences of PIP_3 binding, HDX-MS measurements were taken on P-Rex1 in the presence of
272 liposomes ± PIP_3. Without PIP_3, the most notable changes in P-Rex1 in response to liposomes
273 were increases in protection of the lipid binding elements of both DEP domains (primarily their
274 β1/β2 loops; Sup. Fig. 8A, Sup. Data 2), which suggests that they directly interact with lipid
275 bilayers. Indeed, the isolated DEP1 can independently bind negatively charged liposomes (Ravala
276 et al., 2020). Within the PH domain, there was deprotection of the αC helix, but there was no
277 deprotection at the PH–4HB interface, suggesting that it remained intact. In contrast, membranes
278 with PIP_3 caused deprotection of the entire DH domain, the α6-αN linker and the helices at the
279 DH–DEP1 interface (Fig. 6A, Sup. Fig. 8B, Sup. Data 2). Although the core of the PH domain
280 showed, as expected, an increase in protection in the presence of PIP_3, the structural elements
281 contacting 4HB became deprotected, as did the PH-binding regions of 4HB. Collectively, these
282 data are consistent with loosening of interdomain contacts and unraveling of at least some fraction
283 of P-Rex1 onto the surface of the liposome.
284
285 **Discussion**
286 Here, we showed that IP_4 binding to the PIP_3-binding site in full-length P-Rex1 stabilizes
287 a closed, autoinhibited conformation of P-Rex1 by enhancing long-range contacts across the length
288 of the protein. DH–DEP1 and PH–4HB interactions are relieved upon P-Rex1 binding to PIP_3-
289 containing liposomes, leading to its activation. Canonically, PIP_3 signaling is negatively regulated

290 by PIP_3 phosphatases such as PTEN. Additionally, inositol phosphates, including IP_7 and IP_4, can
291 compete with PIP_3 binding to PH domains (Jia et al., 2007), representing another form of negative
292 regulation. Ins(1,3,4,5)P_4 is a major isoform of IP_4 in neutrophils (Stuart et al., 1994) where its
293 concentration is estimated to be 4 μM (French et al., 1991) and where P-Rex1 is highly expressed
294 (Welch et al., 2002). Because we can measure significant inhibition of P-Rex1 by IP_4 at > 1 μM
295 (Fig. 1D), IP_4 may exert biologically relevant control of Rac activation, at least in neutrophils.
296 Since P-Rex1 can bind membranes in the absence of PIP_3 or Gβγ, IP_4 may serve to suppress P-
297 Rex1 activity until a threshold concentration of PIP_3 is generated, allowing rapid activation of
298 already membrane-associated P-Rex1. It is worth noting that this regulation by specific inositol
299 phosphates may depend on the intracellular distribution of the enzymes responsible for their
300 synthesis (Gokhale et al., 2011).

301 Another key result of our study was to provide a molecular explanation for how the PH
302 and DEP1 domains contribute to P-Rex1 regulation. Nearly two decades ago, it was first reported
303 that domains located C-terminal to the DH domain contribute to P-Rex1 autoinhibition (Hill et al.,
304 2005). Deletion of the PH domain in P-Rex1 resulted in a large increase in activity in the context
305 of the full-length enzyme. However, the DH/PH fragment has higher activity than DH/PH-DEP1
306 and larger P-Rex1 fragments, indicating that the PH domain itself is not intrinsically inhibitory, as
307 it is in some other RhoGEF DH/PH tandems (Bandekar et al., 2019; Chen et al., 2020)(Ravala and
308 Tesmer, 2023). This apparent contradiction can now be explained by the fact that in DH/PH-DEP1
309 and larger fragments, the DH/PH module can jack-knife and position the PH domain in a manner
310 that blocks GTPase binding. This model of regulation was corroborated by recent structural studies
311 of P-Rex1 without IP_4 (Chang et al., 2022). The isolated DEP1 domain was also shown to play an
312 autoinhibitory role based on the relatively low activity of DH/PH-DEP1 relative to DH/PH (Ravala

313 et al., 2020). This can now be explained by its interaction with the DH domain, which,
314 consequently, positions the PH domain to block access of GTPases. Because the PH and DEP1
315 domains can mediate inhibition in the contexts of both DH/PH-DEP1 and the full-length enzyme,
316 and because there is little GEF activity when the DH–DEP1 interface is intact, the DH/PH-DEP1
317 module can be thought of as the core signaling circuit in P-Rex1. In support of this, our mutations
318 in the DH–DEP1 interface were, in general, more activating than those in the PH–4HB interface
319 in cells, although we note that our mutagenesis was not exhaustive (Fig. 5).

320 Using our functional data along with the known structures of P-Rex1, we assembled a
321 model for the activation of P-Rex1 by PIP_3 and Gβγ (Fig. 6B). P-Rex1 in its basal state may be
322 associated with IP_4 and exist in equilibrium at the membrane or in the cytosol. Indeed, in our HDX-
323 MS studies, the DEP1 and DEP2 domains show protection in the presence of liposomes even
324 without PIP_3 (Sup. Fig. 8, Sup. Data 2). In its autoinhibited configuration, the known membrane
325 anchoring elements (the GTPase binding site of the DH domain, the PIP_3-binding site of the PH
326 domain, the β3/β4 loop of the PH domain, the β1/β2 loops of DEP1 and DEP2, and the Gβγ
327 binding site in the C-terminal domains) cannot engage a common membrane plane (Fig. 6B). The
328 clear outlier is the PH domain which would not be able to engage the membrane along with the
329 other domains without unwrapping of the autoinhibited conformation. PIP_3 is not major driver of
330 membrane anchoring on its own (Barber et al., 2007; Cash et al., 2016), and nor is Gβγ, but they
331 do so synergistically in combination (Barber et al., 2007). In prior HDX-MS studies, Gβγ binding
332 did not have a large effect on the regions now known to be involved in autoinhibition and only
333 caused protection in regions of direct contact (Cash et al., 2019). This supports the idea that its
334 role in activation may be primarily related to translocation. This is consistent with the observation
335 that the ΔPH variant of P-Rex1 (which cannot form the DEP1–DH or PH–4HB interfaces or bind

336 PIP_3) is activated to the same extent by Gβγ as WT P-Rex1 (Hill et al., 2005). In autoinhibited P-
337 Rex1, the Gβγ binding site is readily accessible whereas that of PIP_3 is sequestered.
338 We propose that, after stimulation of GPCRs in neutrophils, Gβγ likely binds first and, with
339 the assistance of membrane binding elements in the DEP1 and 2 domains and possibly the β3/β4
340 loop of the PH domain, promotes loosening of the autoinhibited state (Fig. 6B). Generation of PIP_3
341 by PI3K then releases the DH/PH module from the 4HB and DEP1 domain, displacing any bound
342 IP_4. Because neither PIP_3 nor IP_4 can activate DH/PH-DEP1 GEF activity on a soluble GTPase
343 (Sup. Fig. 1A&B), we speculate that this unwrapping at the membrane with multiple points of
344 engagement across the protein is necessary for full activation of P-Rex1 (Fig. 6B). Indeed, our
345 HDX-MS and SAXS studies here support that fully activated P-Rex1 at the membrane will be
346 more extended and dynamic, making the DH domain more accessible to Rac1. However, what
347 remains unknown is the mechanism by which the PH domain is able to access PIP_3 at the
348 membrane, even in a "loosened" autoinhibited state. Furthermore, additional layers of P-Rex1
349 regulation exist that remain underexplored. For example, phosphorylation of the lipid binding loop
350 of DEP1 by PKA is known to inhibit P-Rex1 (Chávez-Vargas et al., 2016; Ravala et al., 2020).
351 Also, a potential interaction may occur between the basic β3/β4 loop of the PH domain and the
352 loop at the end of the 4HB (Fig. 2C). Both loops, consistent with their extended and dynamic
353 nature, have predicted and confirmed phosphorylation sites (Barber et al., 2012) and thus could
354 potentially modulate P-Rex1 activity if they interact. Phosphorylation of the basic β3/β4 loop
355 might be expected to inhibit activity based on the fact that it binds and localizes the protein to the
356 negatively charged plasma membrane, consistent with dephosphorylation of the loop leading to
357 activation (Montero et al., 2016, 2013).
358

359 **Materials and Methods**

360 *Cloning and site-directed mutagenesis*

361 Full-length human P-Rex1, Cdc42 and DH/PH-DEP1 expression constructs were described
362 previously (Cash et al., 2019, 2016; Ravala et al., 2020). Mutations in DH/PH-DEP1 were created
363 using QuikChange (Qiagen) and confirmed by DNA sequencing. Mutations in the pCEFL-HA-
364 HaloTag-P-Rex1 WT construct were created by QuikChange II site-directed mutagenesis (Agilent
365 200523). All constructs were confirmed by sequencing and expression was tested by immunoblot.

366 *Protein purification*

367 Full-length P-Rex1 was transiently expressed in Freestyle 293-F cells and purified as discussed
368 previously (Cash et al., 2019). Briefly, 48 h after transfection, the cells were harvested and lysed
369 with Cell Lytic M (Sigma). After ultracentrifugation to remove the insoluble fraction, the protein
370 was purified using glutathione agarose resin (Gold Biotechnology Inc.). The protein was subjected
371 to TEV cleavage to remove the GST tag and then further purified using a Mono Q 5/50 GL anion
372 exchange column (GE Healthcare Life Sciences). Finally, the protein was purified over an affinity
373 column generated by conjugating human Rac1 to Affi-Gel 10 resin, although for Krios cryo-EM
374 and HDX-MS experiments, this step was omitted.

375 P-Rex1 DH/PH-DEP1 proteins were expressed and purified as described previously
376 (Ravala et al., 2020). Briefly, His-tagged protein was expressed in *E. coli* BL21(DE3) cells which
377 were then lysed using an Avestin Emulsiflex-C3 high-pressure homogenizer. The cell lysate was
378 clarified with high-speed centrifugation, the supernatant was collected, and protein was purified
379 using Ni-NTA resin. The protein was subjected to TEV cleavage to remove the tag. The protein
380 was then purified using a HiTrap SP sepharose column, concentrated, and subjected to size

381 exclusion chromatography on a Superdex S75 column (GE Healthcare) column. Cdc42 was
382 produced in an unprenylated form in *E. coli* and purified as previously described (Cash et al.,
383 2016).

384 *Hydrogen-deuterium exchange mass spectrometry*

385 HDX-MS experiments were performed as previously described (Cash et al., 2019). Briefly,
386 samples were mixed with D_2O buffer to initiate the HDX reaction and, at various time points, the
387 reaction was quenched with ice cold quench buffer and the samples immediately frozen on dry ice.
388 Samples were thawed at 4 °C and subjected to enzymatic digestion on an immobilized pepsin
389 column followed by LC separation and MS analysis. Data were analyzed using HDExaminer
390 (Sierra Analytics, LLC, Modesto, CA). Each sample was analyzed twice by HDX-MS, and the
391 data shown in graphs represent the average of these experiments. Each image in Supplemental
392 Data 1 and 2 shows one experiment (rainbow plots) or a difference analysis from those experiments
393 (red to blue plots). Only one of the two sets of experiments performed for each condition (+/-
394 liposomes or +/- IP4) is shown here. For each peptide, the average of all five time points was
395 calculated and used to plot the difference data onto the coordinates. Coordinates are colored using
396 a range of -20% (darkest blue, protection) to 20% (darkest red, deprotection). P-Rex1 was used at
397 a concentration of 1.7 mg/ml. IP_4 (Cayman Chemical) was added at a concentration of 100 μM.
398 For experiments with liposomes, liposomes were added at a molar ratio of 1 P-Rex1 to 4000 total
399 lipids. Liposomes were composed of 80:80:1 POPC:POPS:PIP_3 and prepared as previously
400 described (Cash et al., 2019).

401 *Guanine-nucleotide exchange assays*

402 Proteins were evaluated for their GEF activity using a fluorescence-based assay (Cash et al., 2019).
403 Briefly, N-methyl-anthraniloyl-GDP (mant-GDP) loaded soluble Cdc42 was used as a substrate
404 GTPase (2 μM) in a buffer containing 20 mM HEPES pH 8, 100 mM NaCl, 0.5 mM $MgCl_2$, 100
405 μM GTP, and reactions were started by addition of P-Rex1 (100 nM). The loss of fluorescence
406 was measured over time at 10 s intervals on a Flexstation 3 plate reader for 40 min. The data was
407 fit to the one-phase exponential decay model in GraphPad Prism with the span (Y_o-plateau) shared
408 among samples. For IP_4 competition curves, GEF assays were carried out in the presence of
409 liposomes containing 2.5 μM PIP_3, as indicated, and 200 μM each of POPC and POPS, prepared
410 as described previously (Cash et al., 2019).

411 *Cryo-EM grid preparation and data collection*

412 For cryo-EM sample preparation, P-Rex1 was used at a final concentration of 3 μM and *n*-dodecyl-
413 β-D-maltoside (DDM) was added to a final concentration of 0.08 mM. For samples with IP_4, a
414 final concentration of 40 μM IP_4 was added. A sample of 4 μl was applied to a glow-discharged
415 Quantifoil (1.2/1.3) 300-mesh grid which was then blotted with filter paper and plunge-frozen into
416 liquid ethane cooled with liquid nitrogen using a Vitrobot Mark IV (Thermo Fisher Scientific) set
417 to 4 °C, 100% humidity, 4 second blot, and a force of 10. Micrographs were collected either using
418 Leginon (Suloway et al., 2005) on a Glacios transmission electron microscope (Thermo Fisher
419 Scientific) operating at 200 keV and a K2 Summit direct electron detector (Gatan, Inc.) in counting
420 mode (0.98 Å/pixel) at a nominal magnification of 45,000x or using EPU (Thermo Fisher
421 Scientific) on a Titan Krios transmission electron microscope (Thermo Fisher Scientific) operating
422 at 300 keV and a K3 direct electron detector (Gatan, Inc.) in counting mode (1.054 Å/pixel) at a
423 nominal magnification of 81,000x. On the Krios, datasets were collected on both untilted and 30°
424 tilted grids (Table 1).

425 *Cryo-EM data processing*

426 To overcome the severe preferred orientation problem of our sample on grids, we collected data
427 on 0˚ and 30˚ tilted samples on a Krios electron microscope and processed these datasets separately
428 up through 2D classification (Table 1). For each dataset, micrograph assessment, particle picking,
429 and contrast transfer function estimation were performed using Warp (Tegunov and Cramer,
430 2019). Particle stacks were taken into CryoSPARC (Punjani et al., 2020, 2017) and extensively
431 cleaned using 2D classification. A final merged particle stack was used for *ab initio* reconstruction
432 into one class followed by non-uniform refinement to obtain a map at an overall 4.1 Å resolution
433 for the P-Rex1·IP_4 complex. For Glacios datasets, data were processed only through 2D
434 classification.

435 *Model building and refinement*

436 Initial model building relied on docking existing atomic models for the DH and PH domains of P-
437 Rex1 (PDB entries 5FL1 and 5D3Y) and the Gβγ-binding scaffold (PDB entry 6PCV). 5D3Y was
438 used for the PH domain because the maps were consistent with IP_4 bound to the PIP_3 site of the
439 PH domain. The DEP1 domain was placed using a non-domain swapped atomic model derived
440 from PDB entry 6VSK. The linker between the PH and DEP1 domains and the 4HB domain were
441 built by hand. A Dali search (Holm and Laakso, 2016) using backbone helices of 4HB revealed its
442 topology to be similar to FAT domains, which was then used to adjust the register of each of its
443 four helices. When Alphafold2 (Jumper et al., 2021) became available, it was used to further adjust
444 the modeling of the 4HB domain and associated structural elements in the IP4P domain. Finally,
445 when the cryo-EM structure of P-Rex1 (PDB entry 7SYF) and the crystal structure of the DH/PH-
446 DEP1 module (PDB entry 7RX9) became available, they were used to confirm less certain regions.

447 Final rounds of real space refinement iterating with manual building were performed in Phenix
448 (Liebschner et al., 2019). Final structure statistics are given in Table 1, and the structure and
449 associated maps were deposited as PDB entry 8TUA and EMDB entry EMD-41621. Raw data
450 were deposited as EMPIAR entry EMPIAR-11967.

451 *Structure visualization*

452 UCSF ChimeraX (Pettersen et al., 2021) was used to make figures showing cryo-EM maps.
453 PyMOL (The PyMOL Molecular Graphics System, Version 2.5.5 Schrödinger, LLC) was used to
454 create all other structure images.

455 *Size exclusion chromatography coupled to small-angle X-ray scattering (SEC-SAXS)*

456 For in solution characterization of DH/PH-DEP1 and its variants, SEC-SAXS was conducted at
457 the BioCAT beamline (Sector18) at the Advanced Photon Source, Argonne National Laboratory
458 using an AKTA Pure FPLC and a Pilatus3 X 1M detector. Purified proteins were injected onto a
459 Superdex 200 Increase 10/300 column at a final concentration of 3-5 mg/ml in 20 mM HEPES,
460 pH 7, 300 mM NaCl, 2% glycerol, and elution from this column flowed into SAXS flow cell for
461 X-ray scattering. Data were collected every 1 s with 0.5 s exposure times at room temperature
462 using 12 KeV X-rays (1.033 Å wavelength) and a 3.67 m sample-to-detector distance. The
463 achievable q range for this experimental setup was (0.0043-0.3546 Å).

464 *SAXS Analysis*

465 The scattering data were processed using BioXTAS RAW 1.6.3 software (Hopkins et al., 2017)
466 (Sup. Fig. 6A) and used to determine the forward scattering I(0) and the radius of gyration, R_g via
467 Guinier analysis (Sup. Fig. 6B). The Kratky plot showed proteins to be flexible (Sup. Fig. 6C)

468 leading to unsuccessful rigid modeling efforts. However, use of the ensemble optimization method
469 (EOM) within ATSAS/3.0.5-2 aided in generating ensembles representing distinct conformational
470 states of the DH/PH-DEP1 fragment and its variants A170K, L177E, and I409A in solution at
471 equilibrium (Ravala et al., 2020). For EOM, the models were generated using crystallographic
472 coordinates from their respective crystal structures: PDB 5FI1 and PDB 6VSK. EOM generated
473 50,000 possible profiles for the full pool using default settings and native-like structures. From
474 these profiles, a sub ensemble that matches the experimental scattering data is selected by a genetic
475 algorithm run 10 times using default settings to verify the stability of the results (results from 1
476 run are shown in Fig. 3E&F). The pair distance distribution function P(r), which provides
477 maximum particle dimension of each protein, was calculated using GNOM (DI, 1992) from the
478 ATSAS 2.8.4 package (Franke et al., 2017) (Sup. Fig. 6D).

479 For quantitative analyses of the flexibility of the selected ensembles, R_{flex} and R_{σ} metrics
480 were derived from EOM data. WT DH/PH-DEP1 and A170K show R_{flex} values smaller than those
481 of the pools, which indicates that these proteins do not exhibit a fully flexible conformation. L177E
482 and I409A variants exhibit R_{flex} values close to those of the pool, suggestive of being highly
483 flexible. Since Guinier analyses and the normalized residual fits of the proteins show that SAXS
484 data quality is good (Sup. Fig. 6B), the R_{σ} value >1 is due to flexibility in the protein, consistent
485 with the EOM analysis (Fig. 3E&F, Sup. Fig. 6A). Results of the SAXS analysis are presented in
486 Table 3 in accordance with the revised guidelines for publishing SAXS data (Trewhella et al.,
487 2017). The SAXS data are deposited in SASBD (https://www.sasbdb.org/) with accession codes
488 SASDUF2 for DH/PH-DEP1 WT, SASDUG2 for DH/PH-DEP1 A170K, SASDUH2 for DH/PH-
489 DEP1 L177E and SASDUJ2 for DH/PH-DEP1 I409A.

490 *Differential scanning fluorimetry*

491 ThermoFluor experiments were performed on a QuantStudio 5 Real-Time PCR system in duplicate
492 with n =3 independent experiments. Purified DH/PH-DEP1 and its variants were incubated at 1
493 mg/ml in a buffer containing 20 mM HEPES pH 7.0, 300 mM NaCl, and 2 mM DTT with 2.5x
494 Sypro Orange dye in a final volume of 10 µl in a 384-well PCR plate. Fluorescence was monitored
495 as a function of temperature, and the T_m was determined by fitting the fluorescence data to a
496 sigmoidal curve and calculating the inflection point in GraphPad Prism.

497 *Luciferase-gene reporter assay*

498 HEK293T cells seeded in 12-wells plates coated with poly-D-lysine were transfected with 500 ng
499 of empty vector pHTN HaloTag CMV-neo (Promega G7721) or pCEFL-HaloTag-P-Rex1
500 constructs and co-transfected with 500 ng of SRE-firefly luciferase and 50 ng of Renilla luciferase
501 plasmids. Thirty-six hours after transfection, the cells were serum-starved overnight and then
502 luminescence signal was measured using Dual-Glo assay system (Promega E2920) according to
503 the manufacturer's instructions. Firefly-luminescence reads were normalized with Renilla-
504 luminescence signal and adjusted to the negative control.

505 *Preparation of P-Rex1 KO in HeLa cells and cell migration assays*

506 HeLa cells were lentiviral transduced with pLentiCRISPRv2 P-Rex1 guide RNA3 -
507 AGGCATTCCTGCATCGCATC (Genscript SC1678). Forty-eight hours after transduction, HeLa
508 cells were selected with puromycin [3 µg/mL] for 7 days. P-Rex1 KO was confirmed by western
509 blot. Chemotactic migration was measured by trans-well assays (Thermoscientific 140629). Inserts
510 of 24-well plates were pre-treated with Fibronectin [50 µg/mL] for 3 hours at 37 °C. Subsequently,
511 $5x10^4$ HeLa cells prepared in serum-free DMEM were plated on the inserts at the upper chamber.
512 Human CXCL12 [50 ng/mL] and EGF [50 ng/mL] (Sigma Aldrich SRP3276 and SRP6253) were

513 prepared in serum-free DMEM and used as chemoattractant in the lower chamber. Serum-free
514 DMEM was used as negative control. The plates with the inserts were incubated in a humidified
515 atmosphere at 37 °C and 5% CO2 for 6 h. After incubation, the cells at the upper surface of the
516 membrane insert were carefully removed and the cells attached to the lower surface were gently
517 washed with PBS and then fixed with 4% paraformaldehyde for 15 min. After fixation, the cells
518 were gently washed with PBS followed by staining with 0.5% crystal violet for 20 min. Excess of
519 crystal violet was removed by gentle PBS washes. Migrating cells were imaged using an inverted
520 microscope. Quantification of particles corresponding to migrating cells was performed with FIJI
521 software.

522 *Western blot*

523 Protein samples prepared in Laemmli buffer were separated with SDS-PAGE using 4-12%
524 gradient gels followed by transfer to PVDF membranes. The membranes were blocked using 5%
525 non-fat milk in TBS-0.05% tween20 (TBST) and incubated overnight at 4 °C with primary
526 antibodies against P-Rex1 and GAPDH (Cell signaling technology #13168 and #5174
527 respectively). The membranes were washed three times with TBST and then incubated with
528 secondary antibodies in blocking solution for 2 h at room temperature. After washing three times
529 with TBST, the reactive bands were visualized using ECL detection reagents and CL-X-posure
530 films.

531 *Statistical analysis*

532 GEF assays described in this study were performed with n>=3 replicates. Statistical significance
533 was determined using one-way ANOVA test with a post hoc Dunnett's test for multiple
534 comparisons.

535 **Acknowledgements**

536 We thank Dr. Srinivas Chakravarthy, Beamline Scientist, for performing SEC-SAXS at BioCAT,
537 Chicago, IL and Dr. Jesse B. Hopkins, Deputy Director, BioCAT for help with SAXS data analysis
538 and interpretation. This research used resources of the Advanced Photon Source,
539 a U.S. Department of Energy (DOE) Office of Science User Facility operated for the DOE Office
540 of Science by Argonne National Laboratory under Contract No. DE-AC02-06CH11357. BioCAT
541 was supported by grant P30 GM138395 from the National Institute of General Medical Sciences
542 of the National Institutes of Health. We thank Dr. Thomas Klose in the Purdue Cryo-EM Facility
543 for technical assistance in cryo-EM data collection. Research reported in this publication was
544 supported by National Institutes of Health grants CA254402, CA221289, HL071818,
545 P30CA023168 (J.J.G.T.), by the Walther Cancer Foundation (J.J.G.T.), and by the National
546 Institute of General Medical Sciences of the National Institutes of Health grant R35GM146664
547 (J.N.C.).

548

549 **Table 1. Cryo-EM data collection, refinement, and validation statistics**

	Structure: P-Rex1–IP_4 (EMDB: EMD-41621) (PDB: 8TUA) (EMPIAR: EMPIAR-11967)	
	Untilted	*Tilted*
Data collection		
Grids	Carbon Quantifoil	Carbon Quantifoil
Vitrification method	FEI Vitrobot	FEI Vitrobot
Microscope	Titan Krios	Titan Krios
Magnification	81000	81000
Voltage (kV)	300	300
Stage tilt (°)	0	30
Detector	K3 DED	K3 DED
Recording mode	Counting	Counting
Total electron exposure (e–/Å^2)	57.8	57.8
Number of frames	40	40
Defocus range (μm)	0.2 – 2.0	0.2 – 2.0
Pixel size (Å)	1.054	1.054
Data processing		
Number of micrographs	2,127	3,069
Initial particle images (no.)	806,067	1,620,545
Final particle images (no.)	89,450	119,739
Initial particle images merged (no.)	209,189	
Final total particle images (no.)	187,734	
Symmetry	C1	
Map resolution (Å)	4.1	
Refinement		
Initial model used (PDB code)	6PCV, 6VSK, 5D3X, 5FI1, 7RX9	
Model resolution (Å)	4.1	
FSC threshold	0.143	
Map sharpening *B* factor (Å^2)	-176	
Model composition		
Non-hydrogen atoms	10,693	
Hydrogens	10,720	
Protein residues	1,330	
Ligands	1 (4IP)	
B factors (Å^2; min/max/mean)		
Protein	30.9/202/123	
Ligand	143/143/143	
R.m.s. deviations		
Bond lengths (Å)	0.003	
Bond angles (°)	0.505	
Validation		
MolProbity score	2.03	
Clashscore	13.88	
Rotamer outliers (%)	0.94	
CaBLAM outliers (%)	2.2	
Ramachandran plot (%)		
Favored	94.5	
Allowed	5.5	
Outliers	0	

Model vs. Data	
CC mask	0.67
CC box	0.73
CC peaks	0.58
CC volume	0.66
Mean CC for ligand	0.67

550

551 **Table 2. Thermofluor measurements of DH/PH-DEP1 variants**

DH/PH-DEP1	T_m (°C)
WT	44.0 ± 0.2
A170K	45.4 ± 0.3 (p<0.0001)
L173A	43.0 ± 0.06 (p<0.0001)
L177A	43.4 ± 0.4 (p=0.0076)
L177E	43.4 ± 0.3 (p=0.0041)
L178A	43.1 ± 0.1 (p<0.0001)
L178E	42.9 ± 0.1 (p<0.0001)
I409A	41.7 ± 0.8 (p<0.0001)
E411K	43.9 ± 0.1 ns[b]
K415A	43.2 ± 0.5 (p=0.0047)
L451A	41.3 ± 0.5 (p<0.0001)
E456K	ND[a]
L466A	ND

From 2 independent experiments performed in triplicate.
P values are from one-way Anova comparisons with WT.
[a] ND: Not determined because inflection point not observed.
[b]ns: nonspecific.

552

553 **Table 3. SAXS parameters for DH/PH-DEP1 variants**

	WT	A170K	L177E	I409A
Guinier Analysis				
I(0)[a]	0.0081 ± 0.00004	0.0021 ± 0.003	0.0092 ± 0.00004	0.0034 ± 0.00002
R_g (Å)	30 ± 0.3	29 ± 0.08	31 ± 0.02	30 ± 0.4
Q_{min} ($Å^{-1}$)	0.0047	0.005	0.0047	0.0047
Q_{max} ($Å^{-1}$)	0.353	0.353	0.353	0.353
P(r) Analysis				
D_{max} (Å)	97	90	110	104
Volume ($Å^3$)	73900	75000	72500	74900
MM_{exp}(MM_{cal}) (kDa)	54 (54)	56 (54)	54 (54)	55 (55)
EOM Analysis				
Crystal Structures	5FI1;6VSK	5FI1;6VSK	5FI1;6VSK	5FI1;6VSK
q-Range ($Å^{-1}$)	.00475-0.353	0.00446-0.353	.00475-0.353	00475-0.353
R_{flex}	70.1% (82.6%)	71.9% (85.3%)	82.9% (84.9%)	79.1% (84.9%)
R_σ	1.18	0.60	1.08	1.56
Skewness	2.39 / 0.41	1.11/ 0.40	0.85 / 0.42	1.50/ 0.40
Kurtosis	4.86/ -0.08	2.09 / -0.14	-0.27 / -0.12	0.77 / -0.14

554 [a] SAXS parameters I(0), R_g, D_{max}, q_{min}, q_{max}, MMexp, MMcal, R_{flex}, R_σ are the
555 experimentally determined intensity at zero scattering angle, radius of gyration,
556 maximum particle dimension, minimum scattering angle, maximum scattering angle,
557 molecular mass calculated from scattering data, molecular mass calculated based on
558 amino acid sequence, flexibility metric of ensemble in comparison (pool value in
559 parentheses), and ratio of standard deviation for the distribution of selected ensemble
560 to that of pool, respectively. The values for EOM analysis are from the last run of the
561 genetic algorithm.

562 **References**

563

564 Bandekar SJ, Arang N, Tully ES, Tang BA, Barton BL, Li S, Gutkind JS, Tesmer JJG. 2019.
565 Structure of the C-terminal guanine nucleotide exchange factor module of Trio in an
566 autoinhibited conformation reveals its oncogenic potential. *Sci Signal* **12**.
567 doi:10.1126/scisignal.aav2449

568 Barber MA, Donald S, Thelen S, Anderson KE, Thelen M, Welch HCE. 2007. Membrane
569 Translocation of P-Rex1 Is Mediated by G Protein beta Subunits and Phosphoinositide 3-
570 Kinase. *Journal of Biological Chemistry* **282**:29967–29976. doi:10.1074/jbc.m701877200

571 Barber MA, Hendrickx A, Beullens M, Ceulemans H, Oxley D, Thelen S, Thelen M, Bollen M,
572 Welch HCE. 2012. The guanine-nucleotide-exchange factor P-Rex1 is activated by protein
573 phosphatase 1α. *The Biochemical journal* **443**:173–183. doi:10.1042/bj20112078

574 Cash JN, Davis EM, Tesmer JJG. 2016. Structural and Biochemical Characterization of the
575 Catalytic Core of the Metastatic Factor P-Rex1 and Its Regulation by PtdIns(3,4,5)P 3.
576 *Structure* **24**:730–740. doi:10.1016/j.str.2016.02.022

577 Cash JN, Urata S, Li S, Ravala SK, Avramova LV, Shost MD, Gutkind JS, Tesmer JJG,
578 Cianfrocco MA. 2019. Cryo–electron microscopy structure and analysis of the P-Rex1–Gβγ
579 signaling scaffold. *Sci Adv* **5**:eaax8855. doi:10.1126/sciadv.aax8855

580 Chang Y-G, Lupton CJ, Bayly-Jones C, Keen AC, D'Andrea L, Lucato CM, Steele JR,
581 Venugopal H, Schittenhelm RB, Whisstock JC, Halls ML, Ellisdon AM. 2022. Structure of
582 the metastatic factor P-Rex1 reveals a two-layered autoinhibitory mechanism. *Nat Struct Mol*
583 *Biol* 1–7. doi:10.1038/s41594-022-00804-9

584 Chávez-Vargas L, Adame-García SR, Cervantes-Villagrana RD, Castillo-Kauil A, Bruystens
585 JGH, Fukuhara S, Taylor SS, Mochizuki N, Reyes-Cruz G, Vázquez-Prado J. 2016. Protein
586 Kinase A (PKA) Type I Interacts with P-Rex1, a Rac Guanine Nucleotide Exchange Factor.
587 *Journal of Biological Chemistry* **291**:6182–6199. doi:10.1074/jbc.m115.712216

588 Chen M, Pan H, Sun L, Shi P, Zhang Y, Li L, Huang Y, Chen J, Jiang P, Fang X, Wu C, Chen Z.
589 2020. Structure and regulation of human epithelial cell transforming 2 protein. *Proc Natl*
590 *Acad Sci* **117**:1027–1035. doi:10.1073/pnas.1913054117

591 Dorseuil O, Vazquez A, Lang P, Bertoglio J, Gacon G, Leca G. 1992. Inhibition of superoxide
592 production in B lymphocytes by rac antisense oligonucleotides. *J Biol Chem* **267**:20540–
593 20542. doi:10.1016/s0021-9258(19)36716-x

594 Franke D, Petoukhov MV, Konarev PV, Panjkovich A, Tuukkanen A, Mertens HDT, Kikhney
595 AG, Hajizadeh NR, Franklin JM, Jeffries CM, Svergun DI. 2017. ATSAS 2.8: a

596 comprehensive data analysis suite for small-angle scattering from macromolecular solutions.
597 *J Appl Crystallogr* **50**:1212–1225. doi:10.1107/s1600576717007786

598 French PJ, Bunce CM, Stephens LR, Lord JM, McConnell FM, Brown G, Creba JA, Michell
599 RH. 1991. Changes in the levels of inositol lipids and phosphates during the differentiation of
600 HL60 promyelocytic cells towards neutrophils or monocytes. *Proc R Soc Lond Ser B: Biol Sci*
601 **245**:193–201. doi:10.1098/rspb.1991.0109

602 Gokhale NA, Zaremba A, Shears SB. 2011. Receptor-dependent compartmentalization of
603 PPIP5K1, a kinase with a cryptic polyphosphoinositide binding domain. *Biochem J* **434**:415–
604 426. doi:10.1042/bj20101437

605 Hayashi I, Vuori K, Liddington RC. 2002. The focal adhesion targeting (FAT) region of focal
606 adhesion kinase is a four-helix bundle that binds paxillin. *Nat Struct Biol* **9**:101–106.
607 doi:10.1038/nsb755

608 Hill K, Krugmann S, Andrews SR, Coadwell WJ, Finan P, Welch HCE, Hawkins PT, Stephens
609 LR. 2005. Regulation of P-Rex1 by phosphatidylinositol (3,4,5)-trisphosphate and
610 Gbetagamma subunits. *The Journal of biological chemistry* **280**:4166–4173.

611 Holm L, Laakso LM. 2016. Dali server update. *Nucleic Acids Res* **44**:W351–W355.
612 doi:10.1093/nar/gkw357

613 Hopkins JB, Gillilan RE, Skou S. 2017. BioXTAS RAW: improvements to a free open-source
614 program for small-angle X-ray scattering data reduction and analysis. *J Appl Crystallogr*
615 **50**:1545–1553. doi:10.1107/s1600576717011438

616 Jia Y, Subramanian KK, Erneux C, Pouillon V, Hattori H, Jo H, You J, Zhu D, Schurmans S,
617 Luo HR. 2007. Inositol 1,3,4,5-Tetrakisphosphate Negatively Regulates Phosphatidylinositol-
618 3,4,5- Trisphosphate Signaling in Neutrophils. *Immunity* **27**:453–467.
619 doi:10.1016/j.immuni.2007.07.016

620 Jumper J, Evans R, Pritzel A, Green T, Figurnov M, Ronneberger O, Tunyasuvunakool K, Bates
621 R, Žídek A, Potapenko A, Bridgland A, Meyer C, Kohl SAA, Ballard AJ, Cowie A, Romera-
622 Paredes B, Nikolov S, Jain R, Adler J, Back T, Petersen S, Reiman D, Clancy E, Zielinski M,
623 Steinegger M, Pacholska M, Berghammer T, Bodenstein S, Silver D, Vinyals O, Senior AW,
624 Kavukcuoglu K, Kohli P, Hassabis D. 2021. Highly accurate protein structure prediction with
625 AlphaFold. *Nature* **596**:583–589. doi:10.1038/s41586-021-03819-2

626 Liebschner D, Afonine PV, Baker ML, Bunkóczi G, Chen VB, Croll TI, Hintze B, Hung L-W,
627 Jain S, McCoy AJ, Moriarty NW, Oeffner RD, Poon BK, Prisant MG, Read RJ, Richardson
628 JS, Richardson DC, Sammito MD, Sobolev OV, Stockwell DH, Terwilliger TC, Urzhumtsev
629 AG, Videau LL, Williams CJ, Adams PD. 2019. Macromolecular structure determination
630 using X-rays, neutrons and electrons: recent developments in Phenix. *Acta Crystallogr Sect D*
631 **75**:861–877. doi:10.1107/s2059798319011471

632 Lucato CM, Halls ML, Ooms LM, Liu H-J, Mitchell CA, Whisstock JC, Ellisdon AM. 2015. The
633 Phosphatidylinositol (3,4,5)-trisphosphate-dependent Rac Exchanger 1:Ras-related C3
634 Botulinum Toxin Substrate 1 (P-Rex1:Rac1) Complex Reveals the Basis of Rac1 Activation
635 in Breast Cancer Cells. *Journal of Biological Chemistry*. doi:10.1074/jbc.m115.660456

636 Mayeenuddin LH, McIntire WE, Garrison JC. 2006. Differential sensitivity of P-Rex1 to
637 isoforms of G protein betagamma dimers. *The Journal of biological chemistry* **281**:1913–
638 1920. doi:10.1074/jbc.m506034200

639 Montero JC, Seoane S, García-Alonso S, Pandiella A. 2016. Multisite phosphorylation of P-
640 Rex1 by protein kinase C. *Oncotarget* **7**:77937–77949. doi:10.18632/oncotarget.12846

641 Montero JC, Seoane S, Pandiella A. 2013. Phosphorylation of P-Rex1 at serine 1169 participates
642 in IGF-1R signaling in breast cancer cells. *Cellular Signalling* **25**:2281–2289.
643 doi:10.1016/j.cellsig.2013.07.018

644 Pettersen EF, Goddard TD, Huang CC, Meng EC, Couch GS, Croll TI, Morris JH, Ferrin TE.
645 2021. UCSF ChimeraX: Structure visualization for researchers, educators, and developers.
646 *Protein Sci* **30**:70–82. doi:10.1002/pro.3943

647 Punjani A, Rubinstein JL, Fleet DJ, Brubaker MA. 2017. cryoSPARC: algorithms for rapid
648 unsupervised cryo-EM structure determination. *Nat Methods* **14**:290–296.
649 doi:10.1038/nmeth.4169

650 Punjani A, Zhang H, Fleet DJ. 2020. Non-uniform refinement: adaptive regularization improves
651 single-particle cryo-EM reconstruction. *Nat Methods* **17**:1214–1221. doi:10.1038/s41592-
652 020-00990-8

653 Ravala SK, Hopkins JB, Plescia CB, Allgood SR, Kane MA, Cash JN, Stahelin RV, Tesmer JJG.
654 2020. The first DEP domain of the RhoGEF P-Rex1 autoinhibits activity and contributes to
655 membrane binding. *J Biol Chem* **295**:12635–12647. doi:10.1074/jbc.ra120.014534

656 Stuart JA, Anderson KL, French PJ, Kirk CJ, Michell RH. 1994. The intracellular distribution of
657 inositol polyphosphates in HL60 promyeloid cells. *Biochem J* **303**:517–525.
658 doi:10.1042/bj3030517

659 Suloway C, Pulokas J, Fellmann D, Cheng A, Guerra F, Quispe J, Stagg S, Potter CS, Carragher
660 B. 2005. Automated molecular microscopy: The new Leginon system. *J Struct Biol* **151**:41–
661 60. doi:10.1016/j.jsb.2005.03.010

662 Tegunov D, Cramer P. 2019. Real-time cryo–EM data pre-processing with Warp. *Nat methods*
663 **16**:1146–1152. doi:10.1038/s41592-019-0580-y

664 Trewhella J, Duff AP, Durand D, Gabel F, Guss JM, Hendrickson WA, Hura GL, Jacques DA,
665 Kirby NM, Kwan AH, Pérez J, Pollack L, Ryan TM, Sali A, Schneidman-Duhovny D,
666 Schwede T, Svergun DI, Sugiyama M, Tainer JA, Vachette P, Westbrook J, Whitten AE.

667 2017. 2017 publication guidelines for structural modelling of small-angle scattering data from
668 biomolecules in solution: an update. *Acta Crystallogr Sect D* **73**:710–728.
669 doi:10.1107/s2059798317011597

670 Tria G, Mertens HDT, Kachala M, Svergun DI. 2015. Advanced ensemble modelling of flexible
671 macromolecules using X-ray solution scattering. *IUCrJ* **2**:207–217.
672 doi:10.1107/s205225251500202x

673 Urano D, Nakata A, Mizuno N, Tago K, Itoh H. 2008. Domain-domain interaction of P-Rex1 is
674 essential for the activation and inhibition by G protein betagamma subunits and PKA.
675 *Cellular Signalling* **20**:1545–1554. doi:10.1016/j.cellsig.2008.04.009

676 Welch HCE, Coadwell WJ, Ellson CD, Ferguson GJ, Andrews SR, Erdjument-Bromage H,
677 Tempst P, Hawkins PT, Stephens LR. 2002. P-Rex1, a PtdIns(3,4,5)P3- and Gbetagamma-
678 regulated guanine-nucleotide exchange factor for Rac. *Cell* **108**:809–821.

679

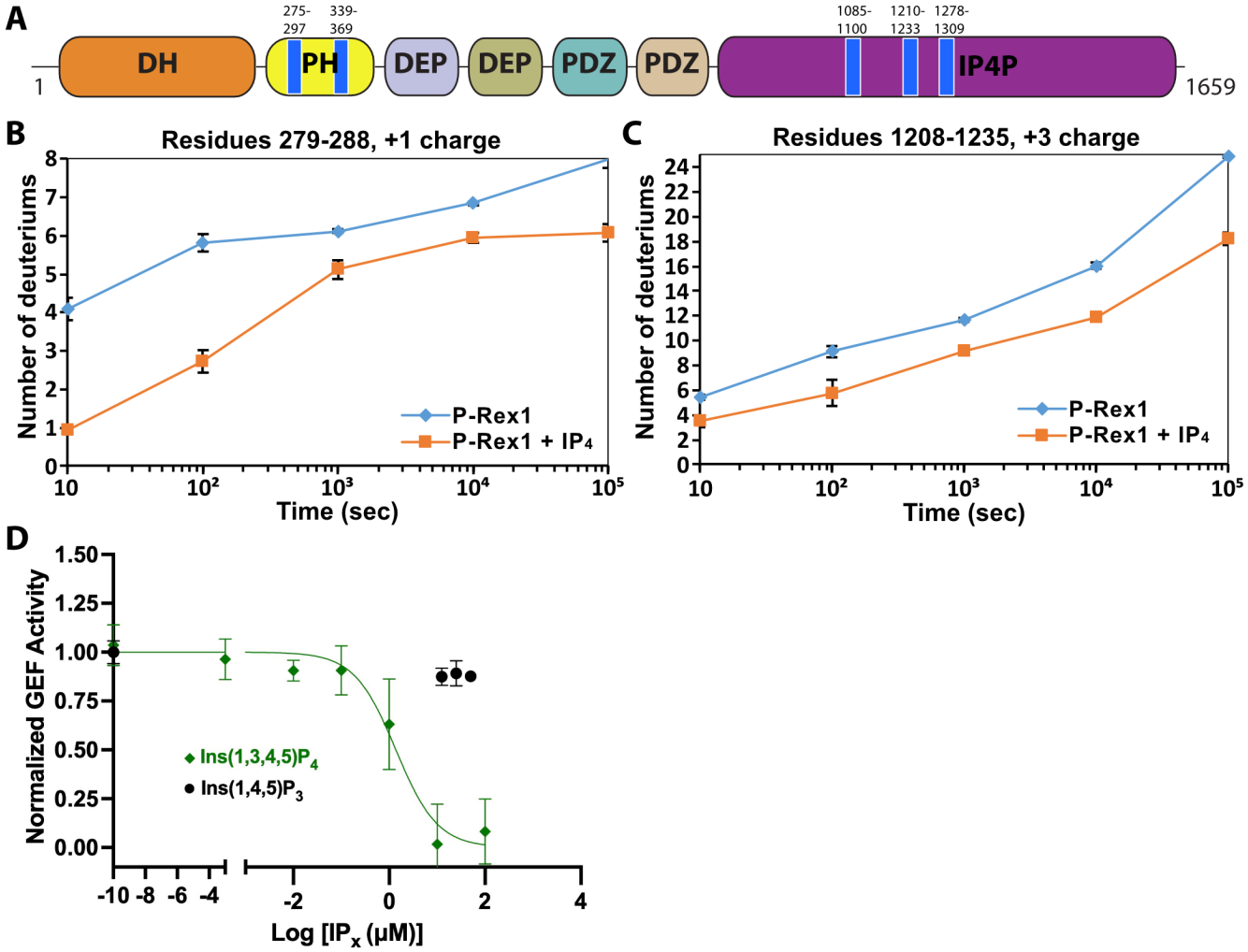

Figure 1. IP_4 binding causes dynamic changes in multiple domains of P-Rex1 and inhibits PIP_3-induced activation. A) Difference HDX-MS data plotted onto the domain layout of P-Rex1. Blue regions indicate less deuterium uptake upon IP_4 binding. Graphs show the exchange over time for select regions in the P-Rex1 (B) PH domain and (C) an IP4P region that was disordered in the P-Rex1–Gβγ structure. The average of two experiments is plotted with the bars representing the range of each time point. D) *In vitro* GEF activity of P-Rex1 evaluated on liposomes containing 2.5 μM PIP_3 in the presence of varying IP_4 concentrations (0-100 μM). Data were fit to exponentials to get rate constants by constraining the span to be shared. The resulting rates for each experiment were normalized by averaging two PIP_3 data points and two PC/PS data points to represent the top and bottom of the binding curve. The resulting normalized rates (min^{-1}) were fit with a one-phase binding curve wherein the top and bottom were constrained to 1 and 0, respectively, and the Hill coefficient fixed at -1. The resulting IC_{50} was 1.4 μM with a confidence interval of 0.81 to 2.3. Data represent 4-5 independent experiments. Error bars represent the mean ± S.D.

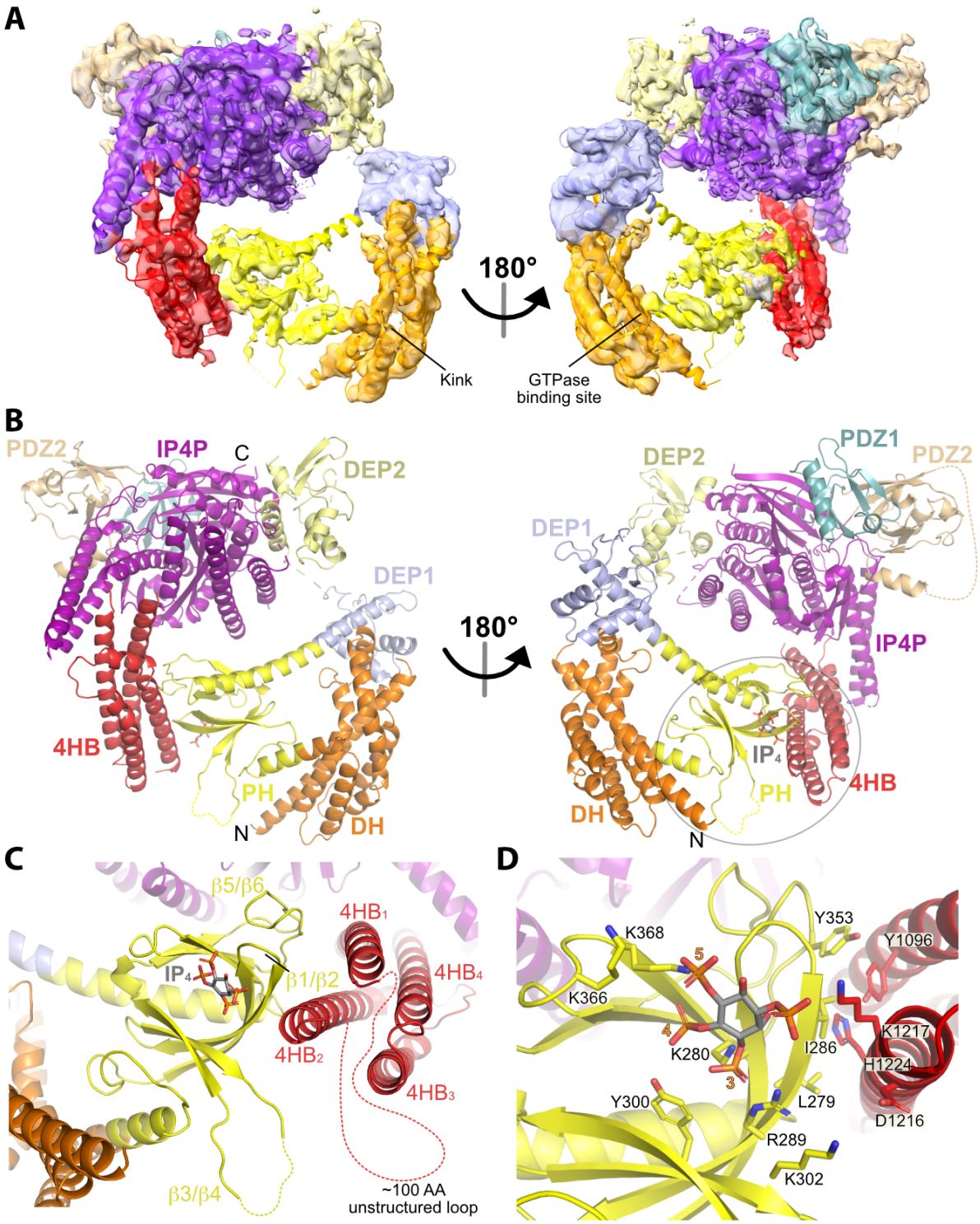

Figure 2. Structure of the P-Rex1·IP_4 complex in an autoinhibited conformation. A) Cryo-EM reconstruction with atomic model superimposed. The kink between the DH and PH domains and the GTPase binding site are labeled. B) Atomic model without the cryo-EM map. C) The PH–4HB interface primarily involves the β1/β2 and β5/β6 loops of the PH domain, which were previously shown to be involved in protein-protein interactions in crystal structures (Cash et al., 2016), and the $4HB_1$ and $4HB_2$ helices of the 4HB domain. Flexible loops, including the basic β3/β4 loop of the PH domain involved in membrane binding (Cash et al., 2016), are shown as dashed lines. We speculate that this loop could interact with phosphorylated residues in the adjacent 4HB unstructured loop. D) Side chains in the PH–4HB interface. The 3-, 4-, and 5-position phosphates of bound IP_4 are labeled. Note that PIP_3 could not bind to the PH domain in this state due to steric blockade by the 4HB domain. The area of focus in (C) and (D) is circled in transparent grey in (B).

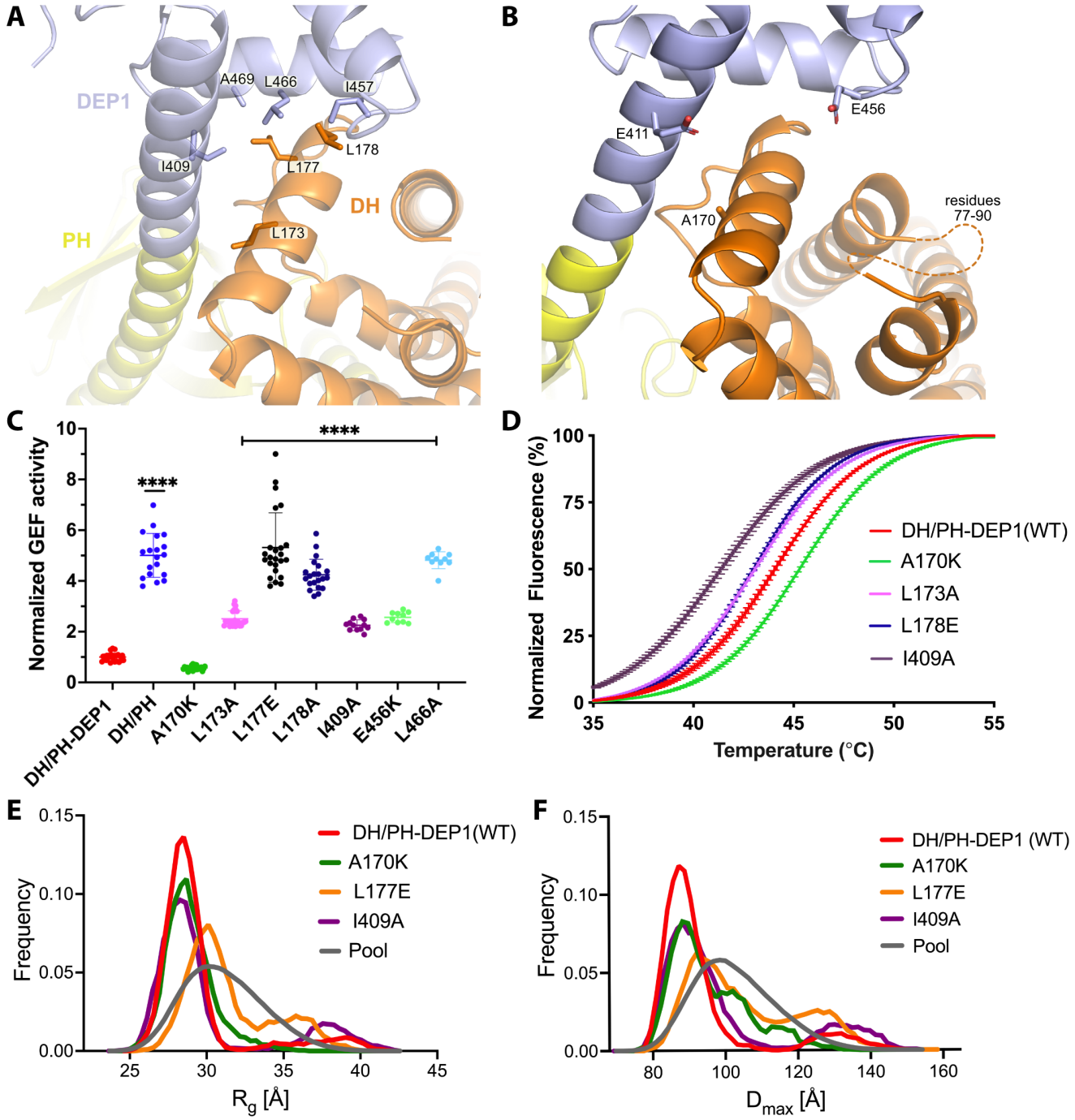

Figure 3. Mutations at the DH–DEP1 interface alter stability, conformation, and activity of DH/PH-DEP1. A) Side chains that contribute to the hydrophobic interface formed between the DH and DEP1 domains. B) Electrostatic interactions contributing the DH–DEP1 interface. The dotted line indicates a disordered region on the DH domain containing positively charged residues that may interact with Glu456. The A170K mutant is expected to form a salt bridge with Glu411 and strengthen the interface. C) Fluorescence based *in vitro* GEF activity assay on soluble Cdc42 with variants of the purified DH/PH-DEP1 fragment. GEF activity in this experiment was fit to a one phase exponential decay normalized to that of DH/PH-DEP1 (WT). ****, P<0.0001. D) Representative Thermofluor analyses showing that mutations that disrupt the DH–DEP1 interface also destabilize the protein, as evidenced by decreased T_m values for each variant (see **Table 2**). Data are normalized from 0-100% representing lowest and highest fluorescence values. Note that A170K, which inhibits activity in panel C, increases stability. E, F) EOM analysis of SAXS data collected from mutations disrupting the DH–DEP1 interface indicate that these variants exhibit more extended conformations (see **Table 3**). EOM analyses provide the R_g and D_{max} distributions derived from selected ensembles. The gray curves correspond to the R_g and D_{max} distributions for the pool of structures used for each analysis.

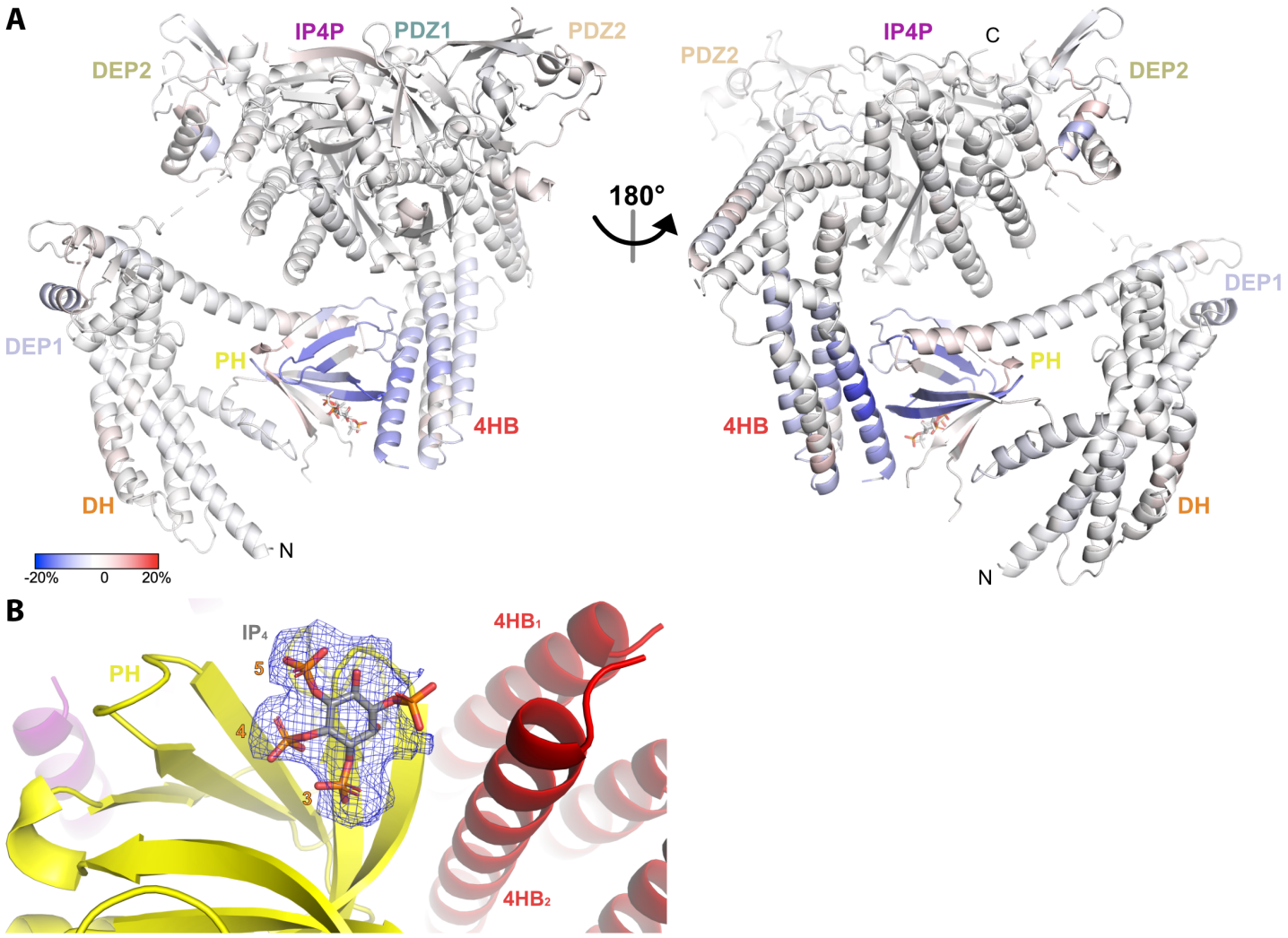

Figure 4. HDX-MS and cryo-EM data support that IP_4 stabilizes a closed conformation of P-Rex1. A) Difference HDX-MS data plotted onto the structure of the P-Rex1 bound to IP_4. Blue regions indicate more protection upon IP_4 binding whereas red regions indicate less. See also Supplemental Data 1. B) Map representing IP_4 bound in the PIP_3-binding site of the PH domain. The 3-, 4-, and 5-phosphates of IP_4 are reasonably well-ordered.

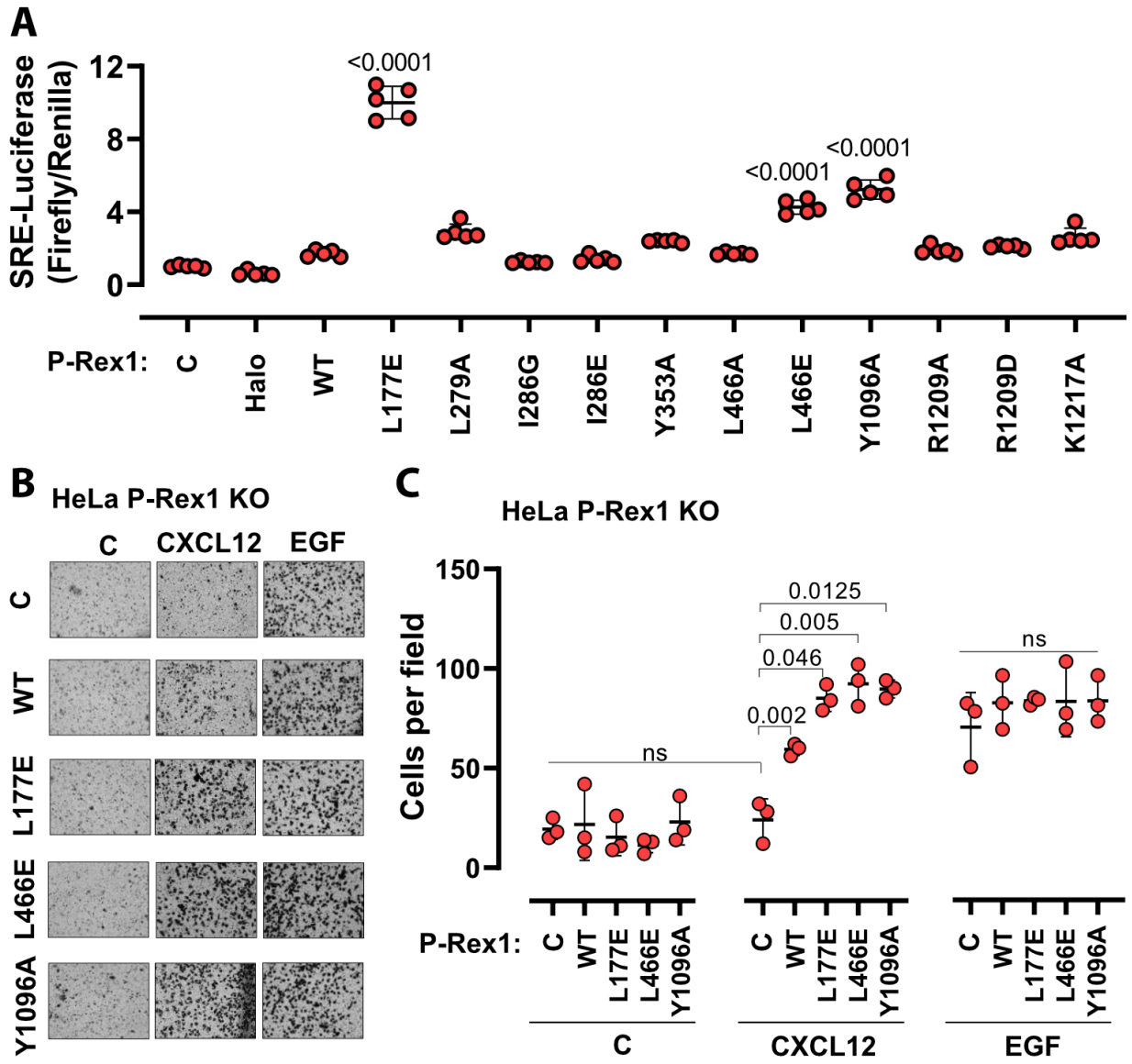

Figure 5. Disruption of the DH–DEP1 and PH–4HB interfaces leads to increased P-Rex1 activity in cells. A) SRE luciferase-gene reporter assays. Mutations were cloned into full-length P-Rex1 in the pCEFL-HA-HaloTag vector, and these constructs, along with luciferase reporter genes, were co-transfected into HEK293T cells. Results depicted here are representative of three independent experiments, and error bars represent S.D. Non-transfected control (C) and empty vector transfected control (Halo) are shown. B) Mutations which led to enhanced P-Rex1 activity in luciferase reporter assays were evaluated for their effect on chemotaxis of HeLa cells with endogenous P-Rex1 knocked out (HeLa P-Rex1 KO; see Supplemental Figure 7). P-Rex1 constructs were transfected into HeLa P-Rex1 KO cells, and cell migration was evaluated in a trans-well migration assay upon stimulation with CXCL12 (50 ng/ml) or EGF (50 ng/ml). Data is presented as mean ± S.D. Significance (brackets) was determined using multiple comparison ANOVA followed by Šidák statistic test.

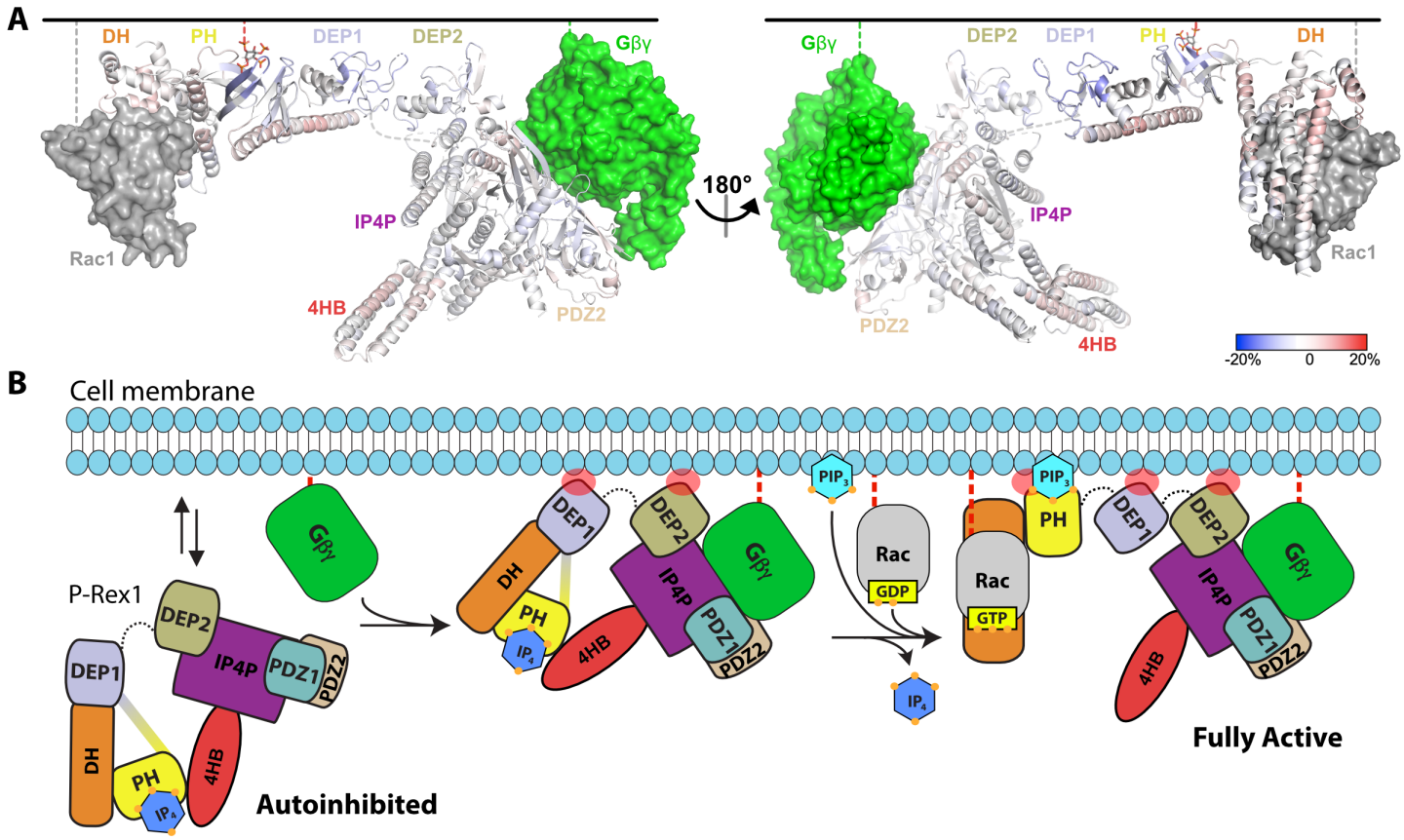

Figure 6. HDX-MS supports that P-Rex1 undergoes long range conformational changes when binding PIP_3-containing liposomes. A) HDX-MS of P-Rex1 in the presence of PIP_3-containing liposomes. A model of P-Rex1 in an open conformation bound to a membrane containing PIP_3 was created and is shown colored according to difference HDX-MS data plotted onto the coordinates. HDX-MS data were collected in the presence of liposomes containing PIP_3 and compared to data collected on P-Rex1 alone. Blue and red regions indicate less and more protection, respectively, upon PIP_3-containing liposome binding. These changes occur specifically in the presence of PIP_3 (see Supplemental Figure 8). The black line at the top represents a membrane surface and the dashed lines represent covalent lipid modifications. Using available structural information, Gβγ and Rac1 were docked into this model (although neither were present in this HDX-MS experiment). B) Cartoon schematic of our model of the steps involved in the activation of P-Rex1.

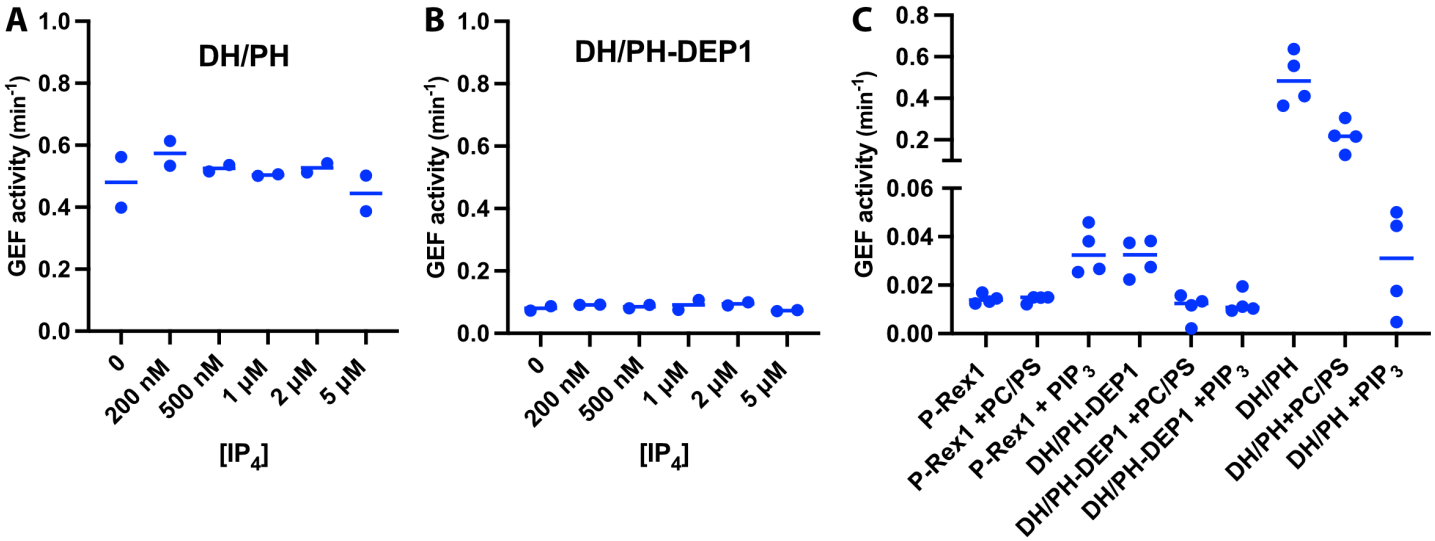

Supplemental Figure 1. P-Rex1 GEF activity assays show that truncated constructs are not inhibited by IP_4 and are not activated by PIP_3-containing liposomes. A and B) Fluorescence-based *in vitro* GEF activity assays with purified P-Rex1 DH/PH and DH/PH-DEP1 proteins (100 nM). Proteins were incubated with varying concentrations (0-5 µM) of IP_4 for 10 min at RT before adding soluble Cdc42 to measure activity. C) *In vitro* GEF activity of full-length P-Rex1, DH/PH, and DH/PH-DEP1 in the absence or presence of liposomes (± 2.5 µM PIP_3). The proteins were incubated with the liposomes for 20 min at RT before adding soluble Cdc42 to measure activity.

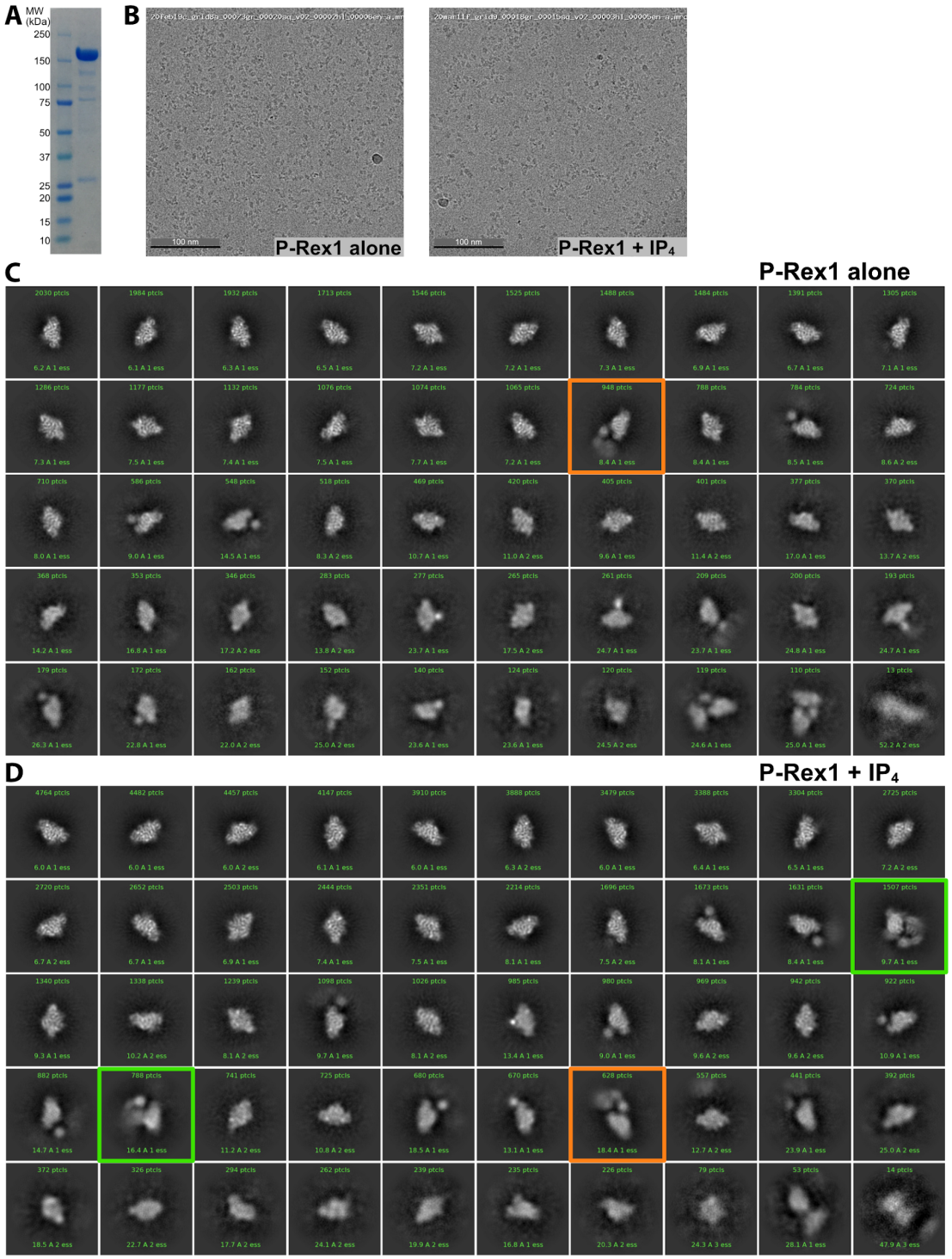

Supplemental Figure 2. Samples of P-Rex1 ± IP_4 imaged on a Glacios microscope highlight a conformation of P-Rex1 that is stabilized by IP_4. A) SDS-PAGE of a sample of purified P-Rex1 that was frozen on grids shown with a molecular weight marker. B) Representative micrographs of P-Rex1 samples. C) Particles of unliganded P-Rex1. These 2D classes represent the best particles (35,302 total) in this data set. D) Particles of P-Rex1·IP_4. These 2D classes represent the best particles (79,378 total) in this data set. 2D classification was performed similarly for the two datasets to select particles that showed the highest resolution features. Pixel size was 1.054 Å, and box size was 288 pixels. Classes that were obviously centered between two separate particles were excluded. Approximately twice as many micrographs were collected for the P-Rex1·IP_4 sample. The number of particles in each class is shown in green text in the box with each class. Orange boxes indicate particles with extra mass to the side of the Gβγ-binding core while green boxes indicate particles with extra mass opposite the Gβγ-binding site on the core.

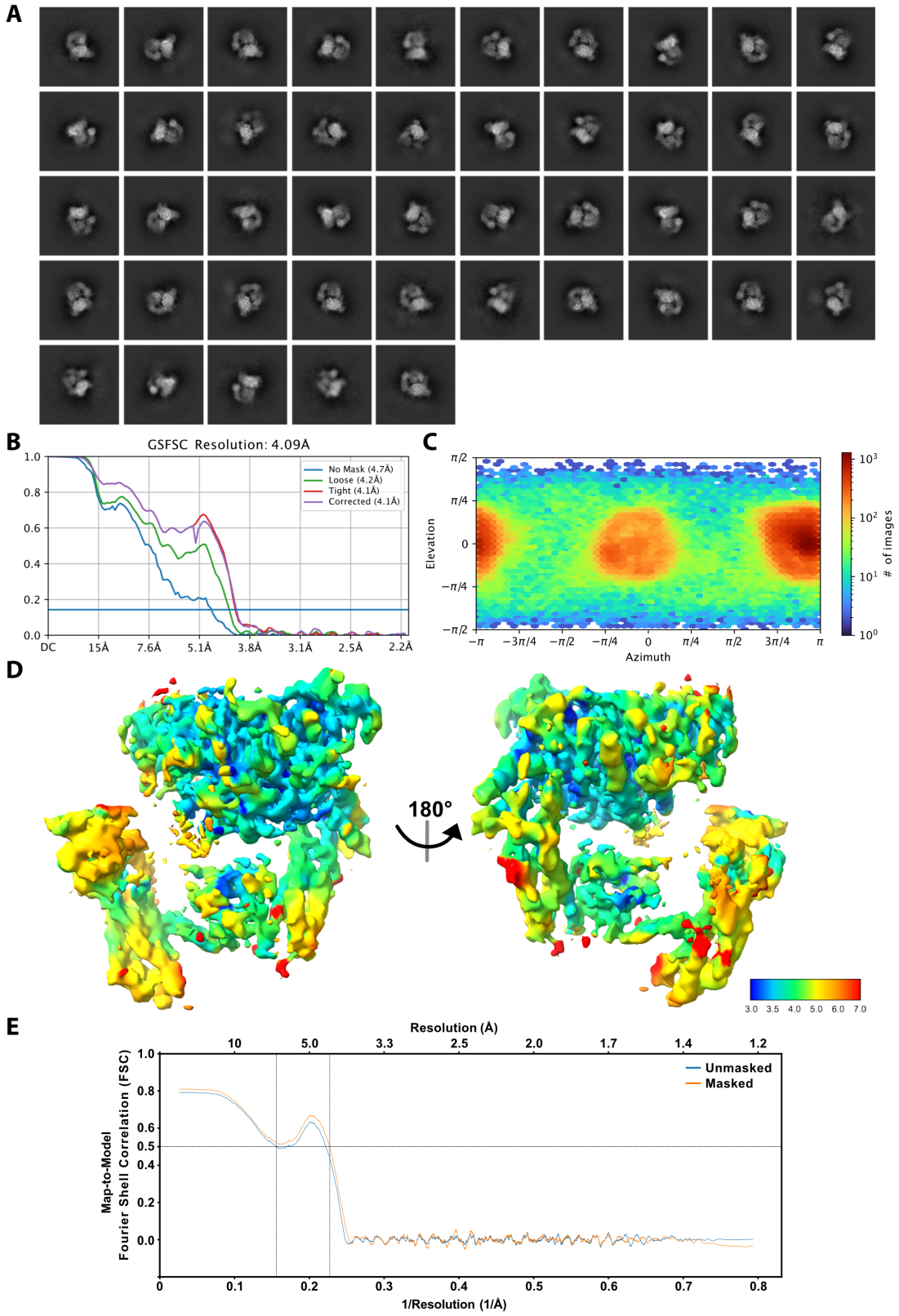

Supplemental Figure 3. Cryo-EM 2D classification and 3D reconstruction. A) 2D class averages of all particles included in the cryo-EM reconstruction. B) Fourier shell correlation (FSC) curve for the final 3D reconstruction. C) Euler angle distribution of the final cryo-EM structure. D) Cryo-EM map of the P-Rex1·IP_4 complex colored according to local resolution calculated by CryoSPARC using a 0.143 FSC cutoff. E) Map-to-model FSC calculated between the atomic model and 3D reconstruction using Phenix showing that the refined model represents the 3D reconstruction.

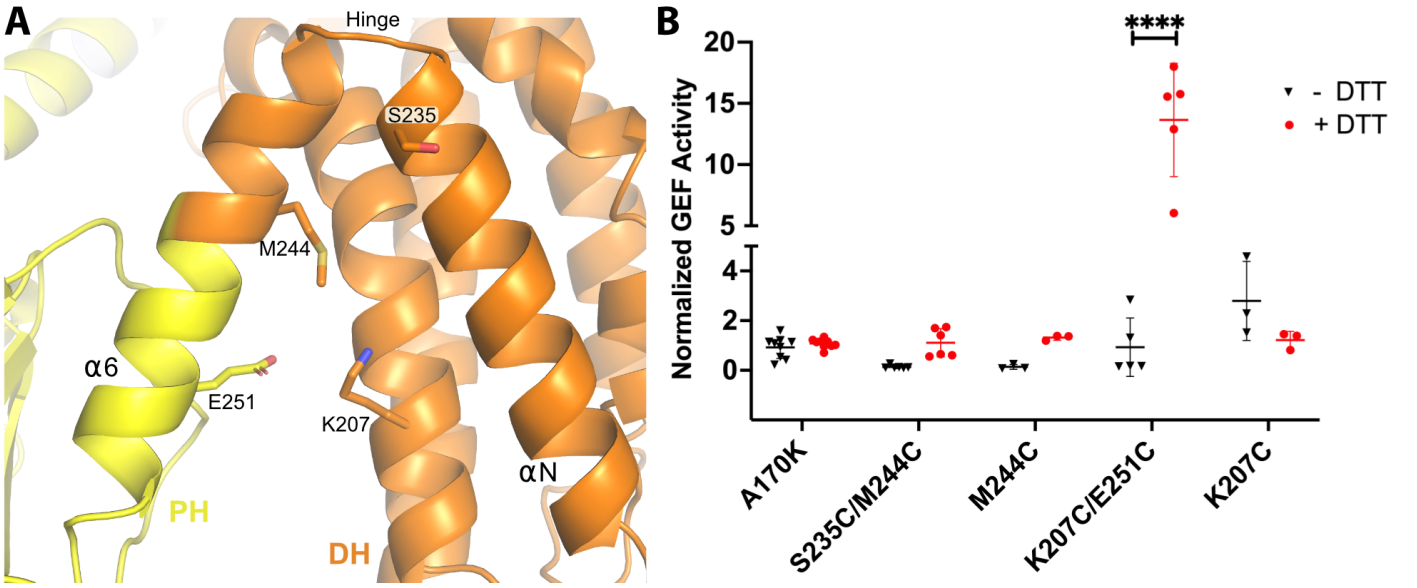

Supplemental Figure 4. Introduction of a disulfide bridge in the DH/PH hinge reduces DH/PH-DEP1 activity. A) Atomic structure of the hinge between the DH and PH domains. Side chains of residues mutated to cysteine are shown. B) GEF activity of DH/PH-DEP1 Cys variants in the background of the A170K mutation. The rate of nucleotide exchange on soluble Cdc42 was normalized to that of the A170K DH/PH-DEP1 variant. Residues were mutated and activities measured under reducing (+DTT) and non-reducing (-DTT) conditions. Similar results were obtained when using $FeCN_6^-$ as an alternative oxidation strategy (data not shown). Data are from at least three independent experiments with error bars representing the mean ± S.D. ****, P<0.0001.

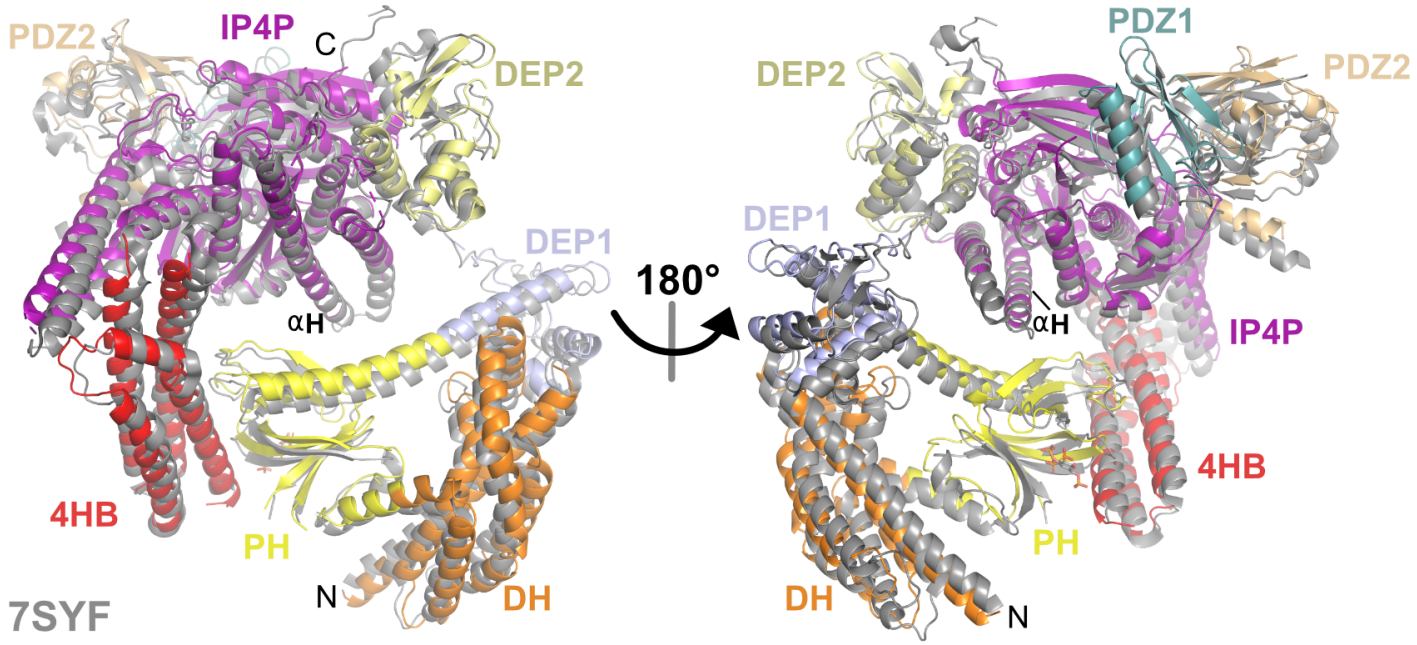

Supplemental Figure 5. The overall structure of the P-Rex1·IP$_4$ complex is similar to that of unliganded P-Rex1. Alignment of the P-Rex1·IP$_4$ complex with the previously determined structure of unliganded P-Rex1 (grey, PDB entry 7SYF). Here, the αH helix of the IP4P domain (residues 1482-1514) in each structure was aligned.

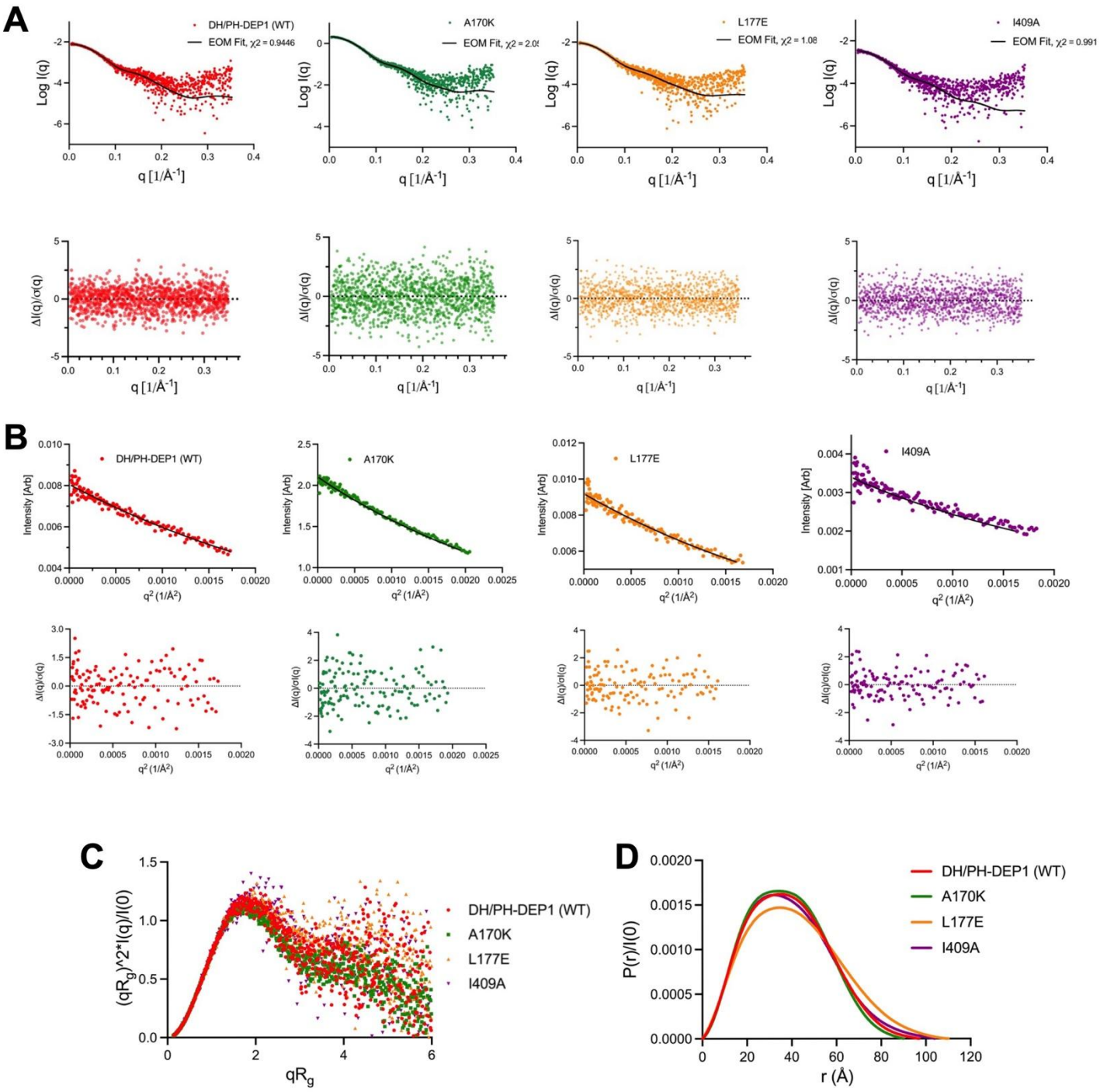

Supplemental Figure 6. SAXS analyses of DH/PH-DEP1 variants. (A) SAXS data (points) and EOM fit (line) for WT DH/PH-DEP1 and variants with mutations at the DH–DEP1 interface. A170K, L177E, and I409A are the variants. Normalized fit residuals are shown in the bottom panel. (B) Guinier analysis with residuals of fit (below). (C) Dimensionless Kratky plots suggest that all the samples have significant degrees of heterogeneity that will not permit rigid body fits. (D) Pair distance distribution (P(r)) functions, normalized by I(0). All curves were nongaussian, indicating the presence of some flexibility or extended conformations.

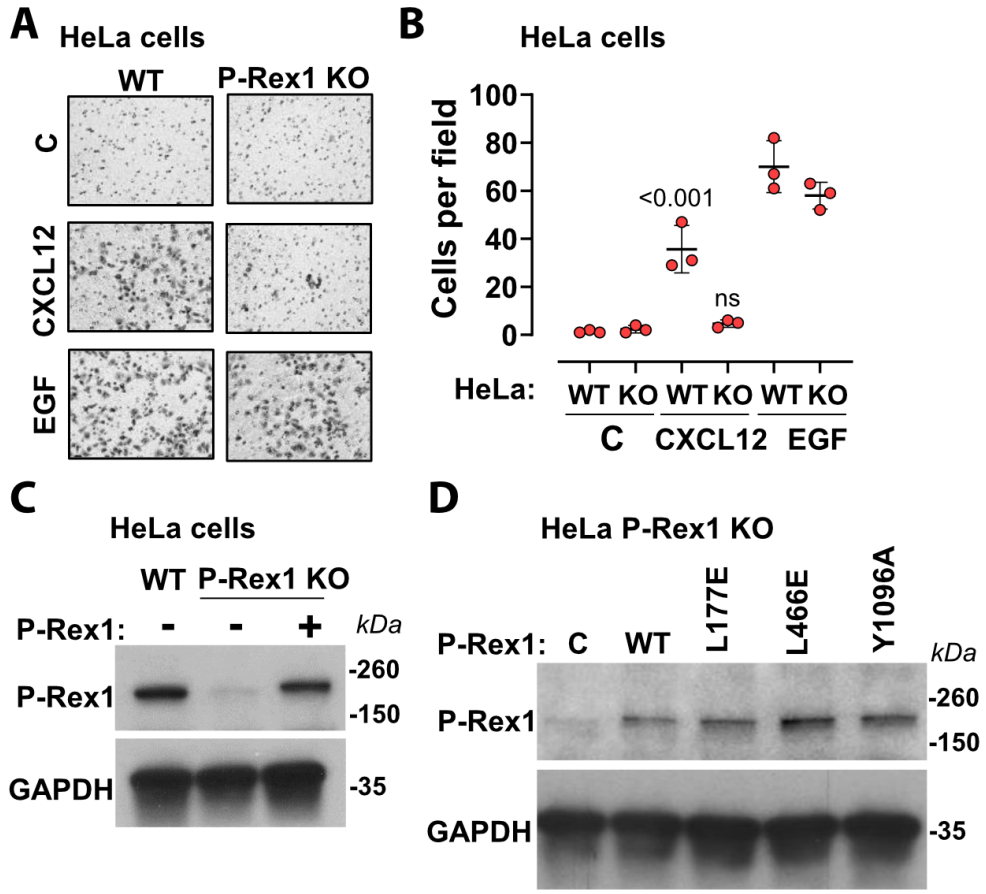

Supplemental Figure 7. P-Rex1 is required for CXCL12-stimulated cell migration downstream of the CXCR4 chemokine receptor. A) Crystal violet staining of trans-well migration inserts showing HeLa cell migration. Chemotaxis was evaluated under conditions without stimulation and after stimulation with CXCL12 (50 ng/mL) or EGF (50 ng/mL) and compared to cells transfected with a WT P-Rex1 construct. B) Quantification of (A), representing results from at least three independent experiments. Error bars show S.D. Significance was determined using Šidák statistic test. C) Western blot analysis of P-Rex1 protein levels in HeLa P-Rex1 KO cells and with wild-type P-Rex1 transfected back in. D) Western blot analysis of P-Rex1 wild-type and variant expression levels in HeLa P-Rex1 KO cells. GAPDH expression level was used as an internal control. P-Rex1 and GAPDH were detected using anti-P-Rex1 and anti-GAPDH antibodies, respectively.

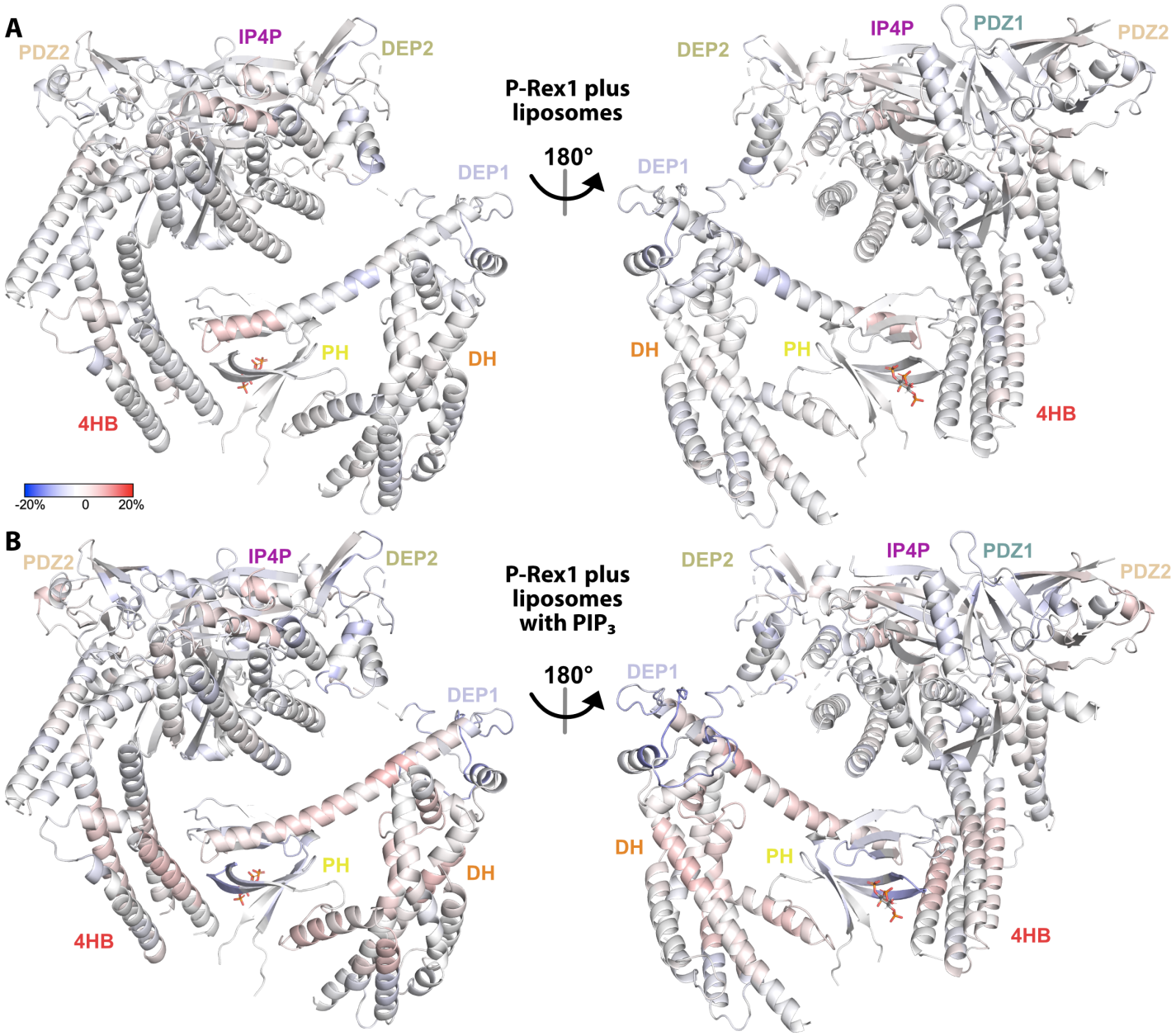

Supplemental Figure 8. Regions across the length of P-Rex1 become more exposed upon binding liposomes specifically containing PIP_3. A) HDX-MS data collected in the presence of liposomes without PIP_3 and compared to data collected on P-Rex1 alone. Blue regions indicate less dynamic behavior or protection upon liposome binding while red regions indicate more. B) HDX-MS data was collected in the presence of liposomes containing PIP_3 and compared to data collected on P-Rex1 alone. Blue regions indicate less dynamic behavior or protection upon PIP_3-containing liposome binding while red regions indicate more. See also Supplemental Data 2.